

Full-scale tsunami-induced scour around a circular pile with three-dimensional seepage

Zhengyu Hu^{ID}, Yuzhu Pearl Li^{ID*}

National University of Singapore, Department of Civil and Environmental Engineering, Singapore

ARTICLE INFO

Keywords:
Tsunamis
Seepage response
Scour
Pile
Sediment transport

ABSTRACT

Seepage flows induced by geophysical tsunamis play a significant role in the tsunami boundary layer dynamics and associated sediment mobility. However, its impact on sediment transport and seabed morphodynamics in the presence of coastal structures remains unclear. In this study, we conduct rigid-bed and morphological simulations to investigate the role of seepage response in full-scale tsunami-induced flow features and sediment transport around a circular pile. The expressions for the onset threshold of sediment transport and the bed load motions are derived considering both bed-slope modifications and three-dimensional seepage forces, which are implemented in the coupled hydrodynamic, morphological, and soil models. The rigid-bed simulations demonstrate that the seabed suction response to the elevation wave can reduce the bed shear stress amplification underneath the contraction of streamlines alongside the pile and lee-wake vortices. The seabed injection response to the depression wave increases the stress amplification. It advances the position of boundary layer separation over the height of the pile, which further changes the lee-wake vortices. Note that the size of the horseshoe vortex and the upward-directed pressure gradient within it are less affected by the seepage flows. In morphological simulations, suspended load transport dominates the scour around the pile. Seabed suction during the elevation wave can slightly reduce the sediment transport rate, decreasing the scour depth, especially at the pile side. Seabed injection during the depression wave causes exacerbated suspended load transport, leading to a more rapid and severe scour at the back of the pile. This study advances the understanding of seepage effects on tsunami-induced sediment transport and scour around a monopile foundation.

1. Introduction

Tsunamis can cause devastating impacts when they reach coastlines, resulting in widespread flooding, destruction of coastal infrastructure, and loss of life (Lynett et al., 2022; Robbe-Saule et al., 2021; Sarlin et al., 2021). The destructive potential of tsunamis extends beyond the immediate impact of the waves. Altered seabed topography, changes in sediment composition, and the redistribution of nutrients can pose threats to infrastructure and impact coastal ecosystems (Dawson and Shi, 2000; Mori et al., 2011; Apotoss et al., 2011; Jayaratne et al., 2016; McGovern et al., 2019). Tsunami field surveys from the 1992 Nicaragua tsunami to the recent 2022 Tonga tsunami have provided valuable insights into the scouring effects on coastal structures and the associated sediment transport dynamics (Satake et al., 1993; Fritz et al., 2007; Lacy et al., 2012; Yeh et al., 2013; Borrero et al., 2023). Understanding these processes is crucial for assessing tsunamis' long-term ecological and geological impacts, informing disaster management strategies, and promoting resilient coastal development in vulnerable regions.

Monopiles are widely used in marine environments for offshore wind farms, oil/gas platforms, and bridge foundations (Gupta and Basu, 2020; Zou et al., 2021; Guan et al., 2022). While there have been numerous studies on scour around piles subjected to waves (Sumer et al., 1992; Sumer and Fredsøe, 2002; Baykal et al., 2017; Chen et al., 2022; Zhang et al., 2023), tidal currents (Roulund et al., 2005; Zhao and Cheng, 2008; Zhao et al., 2010; Baykal et al., 2015; Whitehouse and Stroescu, 2023), and combined waves and current (Sumer and Fredsøe, 2001; Sumer et al., 2013; Qi and Gao, 2014; Chen and Li, 2018; Larsen and Fuhrman, 2023) in past decades, the potential scour induced by the tsunami attack has received relatively little specific attention. Tsunamis are expected to have different scour mechanics from these conventional ocean loads. From the hydrodynamic perspective, tsunamis are characterized by long waves, typically with periods spanning from minutes to hours and wavelengths extending over hundreds of kilometers (Carrier et al., 2003; Madsen et al., 2008; Chan and Liu, 2012; Liu and Higuera, 2022). The tsunami propagation and inundation have been extensively investigated (Sugawara

* Corresponding author.

E-mail addresses: z.hu@u.nus.edu (Z. Hu), pearl.li@nus.edu.sg (Y.P. Li).

et al., 2014; Larsen and Fuhrman, 2019a; Omira et al., 2022; Ren et al., 2023). The studies on the associated boundary layer dynamics are limited but significant for assessing the interaction with the seabed, i.e., sediment transport and morphological process. Williams and Fuhrman (2016) numerically simulated the transient wave boundary layers at full-tsunami scales using a one-dimensional vertical (1DV) Reynolds-averaged Navier–Stokes (RANS) model, which suggests that the boundary layers underneath tsunamis exhibit characteristics akin to currents, owing to their prolonged duration, while also retaining wave-like attributes, as their thickness may not extend across the entire water depth. This aligns with field measurements recorded in northern Monterey Bay during the 2010 Chile tsunami arrival (Lacy et al., 2012), as well as computational fluid dynamics (CFD) simulations conducted on full-scale tsunamis approaching various constant sloped areas (Larsen and Fuhrman, 2019b).

There are limited studies on the tsunami-induced scour around offshore and coastal structures. Wilson et al. (2012) compared the video, bathymetry, and sediment data from harbors in California (USA) before and after the 2011 Tohoku tsunami. They showed significant scour and deposition within the harbors, which could contribute to the weakening foundations and long-term usability problems. Additionally, Bricker et al. (2012) conducted field measurements on the scour depth on the landward side of seawalls and foundation footings induced by the 2011 Tohoku tsunami. Chen et al. (2013) investigated tsunami-induced scour at coastal roadways through experimental studies. Larsen et al. (2017, 2018) numerically and experimentally investigated the tsunami-induced scour around a monopile structure using the standard shear stress descriptions, where the tsunami flow is represented as a time-varying current, and the free-stream velocity is given by either a sinusoidal wave or a single wave (elongated soliton). However, Tonkin et al. (2003) found that the standard shear stress model cannot qualitatively explain the rapid scour at the back of the cylinder under low flow velocity at the end of tsunami draw-down from a large-scale experiment. They showed that the development of pore-pressure gradients in the underlying soil associated with rapid drops in water levels buoys up the superficial sediment, which decreases the onset threshold of the sediment motion. When the pore-pressure gradient exceeds the buoyant weight of the sediment, the effective stress between sediment grains could vanish to form momentary liquefaction, making the sediment readily scoured (Sumer and Fredsøe, 2002; Sumer, 2014; Qi and Gao, 2018; Li et al., 2018, 2020a). The effect of the increased pore-pressure gradient on the tsunami scour process was studied by Nakamura et al. (2008) for a land-based square structure and by Hu et al. (2024) for a submarine pipeline. The tsunami-induced momentary liquefaction was detected in the large-scale experiments of Yoshii et al. (2017, 2018), analytical and numerical solutions (Liu et al., 2007; Tong and Liu, 2022), and the collapse processes of a quay wall in Konakano, Japan, under no ground shaking and low flow velocity during the draw-down period of the 1960 Chilean tsunami, as reported by Yeh and Mason (2014). Understanding the effect of pore-pressure gradients is crucial for accurately estimating tsunami-induced scour.

Recent studies have attempted to reveal the effect of pore-pressure gradients on sediment transport. The incipient motion threshold for sediment particles on a flatbed subjected to the vertical (Guo et al., 2019), two-dimensional (Zhai et al., 2021a; Wang et al., 2024), and three-dimensional seepage forces (Zhai et al., 2021b) were modified from the classic Shields parameter description. The bed-slope modifications on the critical Shields parameter and bed load transportation were further considered in the presence of vertical seepage forces (Cheng and Chiew, 1999; Li et al., 2020a; Hu et al., 2024). However, the general expression considering both bed-slope modifications and three-dimensional seepage forces has not yet been proposed. In addition to seepage forces, the seepage velocities induced by pore-pressure gradients could, in turn, significantly affect the profiles of the near-bed flow velocity and bed shear stresses (Cheng and Chiew, 1998; Chen and Chiew, 2004; Dey and Nath, 2010; Sharma and Kumar,

2017; Li et al., 2020a; Taye et al., 2023). Hu et al. (2024) showed the competing seepage effects on the onset threshold of sediment transport and the bed shear stress, which results in not necessarily increased bed load transport during the tsunami draw-down. However, most previous models addressing seepage effects on sediment transport have overlooked these impacts. The bed shear stress influenced by seepage velocities was not resolved due to the one-way coupling of the model (Guo et al., 2019; Zhai et al., 2021a; Zhai and Jeng, 2024). Incorporating the two-way coupling of wave pressure and soil response such as Zhai and Jeng (2022) and Ye et al. (2024) into the sediment transport and seabed morphological model can better characterize the role of seepage effects on scour. Sui et al. (2024) investigated seabed response and liquefaction around monopile in the context of short waves. The pre-specified scour hole reduces pore pressure and creates a more uniform liquefaction depth around the monopile, which intensifies with higher soil saturation but varies with permeability. The role of seepage response on the flow features and scour around monopiles induced by the tsunami attack has not been previously studied, either experimentally or numerically. In scaled flume experiments, the pore-pressure gradients induced by waves in the surficial seabed are usually much lower than the buoyant weight of the sediment (Qi and Gao, 2014). Moreover, replicating tsunami waves experimentally is indeed challenging due to their prolonged duration. Consequently, it is hard to directly observe the seepage effects on tsunami scour in a laboratory experiment.

In the present study, we conduct full-scale rigid-bed and morphological simulations to investigate the role of seepage response in tsunami-induced flow features and scour around a circular pile. The remainder of the paper is organized as follows. Section 2 presents the onset threshold of sediment transport and the bed load transportation for the particle on a sloping bed subjected to the three-dimensional seepage forces. These are implemented into the coupled hydrodynamic, morphological, and soil models. The model is then validated against the laboratory experiments of a turbulent boundary layer subjected to seepage velocities and tsunami-induced scour around a monopile. Section 3 describes the used full-scale tsunami signal and the corresponding seepage response. Section 4 discusses the main tsunami flow features around a circular pile with and without considering the seepage effects. Section 5 presents the seepage effects on the evolution of tsunami-induced scour. Finally, conclusions are drawn in Section 6.

2. Models and methodologies

In this section, we first derive the onset threshold of sediment transport and the bed load transportation for a particle on a sloping bed subjected to the three-dimensional seepage forces in Sections 2.1 and 2.2. We then present the fully coupled hydrodynamic, morphological, and soil models with further consideration of the dynamic seepage response in Section 2.3. Furthermore, we validate the model against laboratory experiments in Section 2.4. Finally, we show the model setup and boundary conditions for simulating the sediment transport and morphological processes around a circular pile subjected to the tsunami waves in Section 2.5.

2.1. Onset threshold of sediment transport

For flow over a bed composed of cohesionless grains (see Fig. 1), the driving force on a non-moving spherical sediment particle consists of the flow-induced drag force F_D in the flow direction and lift force F_L in excess of the natural buoyancy. Since the lift force has a similar expression as the drag force, the driving force can be given in the following form (Fredsøe and Deigaard, 1992, pp. 201–202)

$$F_D = \frac{1}{2} \rho C_D \frac{\pi}{4} d^2 (aU_f)^2, \quad (1)$$

where ρ is the density of fluid, C_D stands for a drag (and lift) coefficient, d is the median diameter of the particle, U_f is the friction velocity,

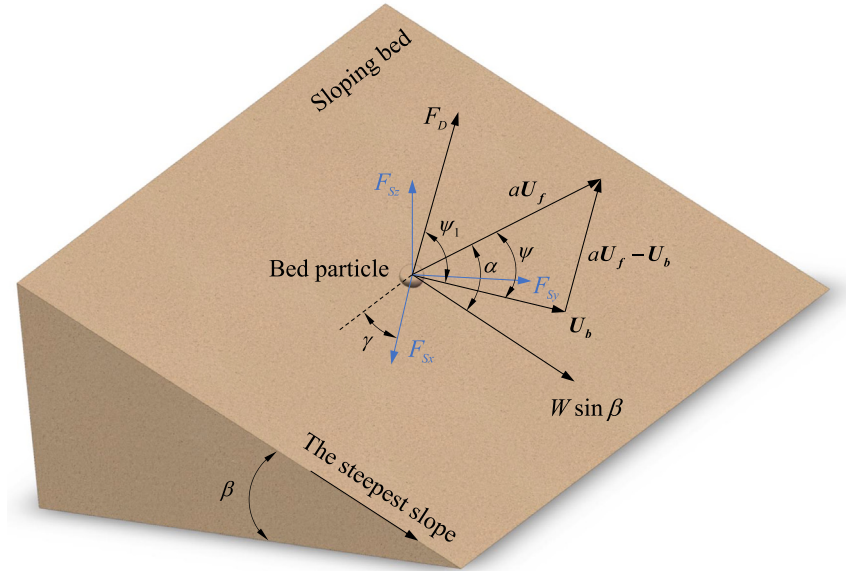


Fig. 1. Force balance on a single moving sediment particle on a sloping bed.

and a is an empirical constant, taken as $a = 10$ (Engelund and Fredsøe, 1976; Roulund et al., 2005). The three-dimensional seepage force $F_S = (F_{Sx}, F_{Sy}, F_{Sz})$ in the Cartesian coordinate system is induced by the pore-pressure gradient at the bed surface, expressed as

$$F_S = \frac{i\rho g\pi d^3}{6(1-n)}, \quad (2)$$

where $i = (i_x, i_y, i_z)$ is the hydraulic gradient at the surficial bed, g is the gravitational acceleration, and n is the porosity of the sediment particles (Cheng and Chiew, 1998). The submerged weight of the particle is given by

$$W = \frac{(s-1)\rho g\pi d^3}{6}, \quad (3)$$

where s denotes the specific gravity. The stabilizing force is the frictional force acting on a particle at rest. The threshold of the incipient sediment motion on a sloping bed is attained when the driving force on the particle is about to exceed the stabilizing force

$$\begin{aligned} & (F_{Dc} \sin \alpha - F_{Sx} \cos \gamma + F_{Sy} \sin \gamma)^2 \\ & + [F_{Dc} \cos \alpha + (W - F_{Sz}) \sin \beta + (F_{Sx} \sin \gamma + F_{Sy} \cos \gamma) \cos \beta]^2 \\ & = \mu_s^2 [(W - F_{Sz}) \cos \beta - (F_{Sx} \sin \gamma + F_{Sy} \cos \gamma) \sin \beta]^2, \end{aligned} \quad (4)$$

where F_{Dc} is the critical drag force, β is the angle of the sloping bed, i.e., the angle between the steepest slope and horizontal plane, α is the angle between the flow velocity vector and the direction of the steepest bed slope, γ is the angle between F_{Sx} and the transverse direction of the bed slope, $\mu_s = \tan \beta_r$ is the static friction coefficient for the sediment, and β_r is the angle of repose. Assuming that the seepage flow marginally influences the static friction coefficient of sediment particles (Zhai and Jeng, 2024), the force balance determines the dimensionless form of the critical bed shear stress, critical Shields parameter θ_c

$$\begin{aligned} \theta_c &= \frac{U_{fc}^2}{(s-1)gd} \\ &= \frac{\theta_{co,i=0}}{\mu_s i_c} \left[A \sin \alpha - B \cos \alpha + \sqrt{(A \sin \alpha - B \cos \alpha)^2 - (A^2 + B^2 - C^2)} \right], \end{aligned} \quad (5)$$

where U_{fc} is the critical friction velocity and $i_c = (s-1)(1-n)$ is the critical hydraulic gradient to cause fluidization of a bed, which is determined by the specific gravity and porosity of sediment grains. $\theta_{co,i=0} = 4\mu_s/3a^2C_D$ is the critical Shields parameter on a flatbed

without seepage flows, which can be obtained from the classic Shields diagram (Fredsøe and Deigaard, 1992, pp. 201–203). The coefficients are given by

$$\left. \begin{aligned} A &= i_x \cos \gamma - i_y \sin \gamma; \\ B &= (i_c - i_z) \sin \beta + (i_x \sin \gamma + i_y \cos \gamma) \cos \beta; \\ C &= \mu_s [(i_c - i_z) \cos \beta - (i_x \sin \gamma + i_y \cos \gamma) \sin \beta]. \end{aligned} \right\} \quad (6)$$

When only the vertical seepage force is considered, i.e., $i_x = 0$ and $i_y = 0$, the critical Shields parameter can be reduced to the expression proposed by Hu et al. (2024)

$$\theta_c = \left(1 - \frac{i_z}{i_c} \right) \left(\cos \beta \sqrt{1 - \frac{\sin^2 \alpha \tan^2 \beta}{\mu_s^2}} - \frac{\cos \alpha \sin \beta}{\mu_s} \right) \theta_{co,i=0}. \quad (7)$$

2.2. Bed load transportation

We extend the bed load transport formulation of Roulund et al. (2005), who extended the well-known transport formulation of Engelund and Fredsøe (1976) to include three-dimensional effects as well as bed-slope modifications, to consider an additional three-dimensional seepage force induced by the pore-pressure gradient in the soil. The bed load formula considers the equilibrium of forces acting on a bed load particle, containing the agitating and the stabilizing forces. When the bed load particles are moving with a mean transport velocity U_b shown in Fig. 1, the agitating force due to the streamwise flow is expressed by (Fredsøe and Deigaard, 1992, p. 210)

$$F_D = \frac{1}{2}\rho C_D \frac{\pi}{4} d^2 U_r^2, \quad (8)$$

where U_r is the relative velocity between the flow and the particle

$$U_r = aU_f - U_b, \quad (9)$$

and C_D can be obtained from the force balance for a bed load particle on a horizontal bed under the critical velocity, which is further modified according to the experimental data (Fredsøe and Deigaard, 1992, p. 211)

$$C_D = \frac{4\mu_d}{3a^2 \left(\frac{1}{2}\theta_{co} \right)}, \quad (10)$$

where μ_d represents the dynamic friction coefficient, $\frac{1}{2}\theta_{co}$ was suggested by Fernandez Luque and Van Beek (1976) from their experimental observations.

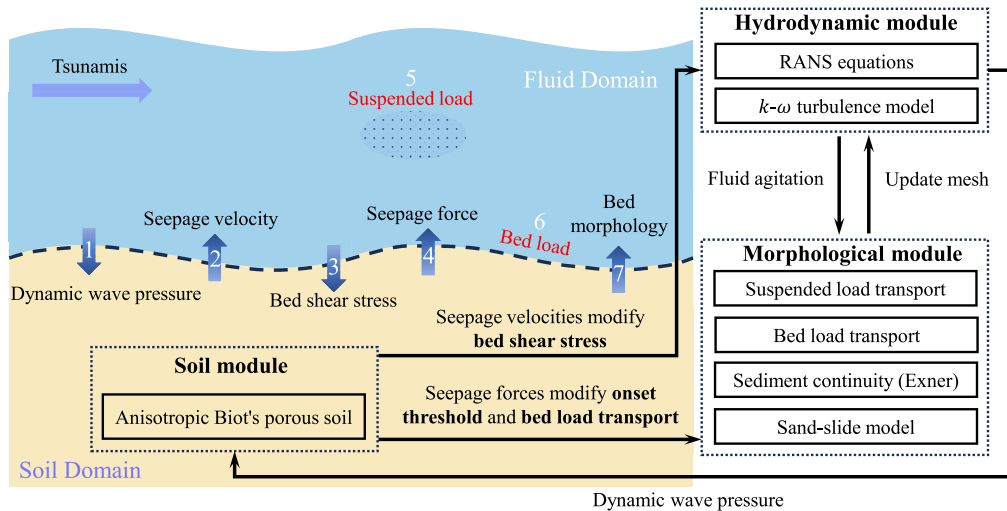


Fig. 2. Sketch and flowchart of the coupled CFD model. The blue arrows represent the data transfer direction, while the numbers denote the solving sequence at each time step. The free surface is shown for illustration only and is not included in the model.

We consider the two components of the equation of the particle motion influenced by the three-dimensional seepage force. Assuming that the particles move at a constant velocity on average U_b , the equation of motion in the direction of the particle motion is:

$$\begin{aligned} F_D \cos \psi_1 + [(W - F_{Sz}) \sin \beta + (F_{Sx} \sin \gamma + F_{Sy} \cos \gamma) \cos \beta] \cos(\alpha - \psi) \\ - (F_{Sx} \cos \gamma - F_{Sy} \sin \gamma) \sin(\alpha - \psi) \\ - \mu_d [(W - F_{Sz}) \cos \beta - (F_{Sx} \sin \gamma + F_{Sy} \cos \gamma) \sin \beta] = 0. \end{aligned} \quad (11)$$

The equation of motion in the direction perpendicular to U_b , on the other hand, reads:

$$\begin{aligned} F_D \sin \psi_1 - [(W - F_{Sz}) \sin \beta + (F_{Sx} \sin \gamma + F_{Sy} \cos \gamma) \cos \beta] \sin(\alpha - \psi) \\ - (F_{Sx} \cos \gamma - F_{Sy} \sin \gamma) \cos(\alpha - \psi) = 0. \end{aligned} \quad (12)$$

There are also the following geometric relations from Fig. 1

$$U_r \sin \psi_1 - aU_f \sin \psi = 0, \quad (13)$$

and

$$U_r \cos \psi_1 - aU_f \cos \psi + U_b = 0. \quad (14)$$

Eqs. (11)–(14) are to be solved for the four unknowns, namely U_b , U_r , ψ , and ψ_1 . The Newton-Raphson technique has solved these equations in full form. Once mean particle velocity U_b is determined, the rate of bed load transport q_b can be determined by (Fredsøe and Deigaard, 1992, p. 211)

$$q_b = \frac{\pi}{6} d^3 \frac{p_{EF}}{d^2} U_b, \quad (15)$$

where p_{EF} is the percentage of the topmost particles in motion, expressed by (Fredsøe and Deigaard, 1992, p. 213)

$$p_{EF} = \left[1 + \left(\frac{\pi \mu_d}{6(\theta - \theta_c)} \right)^4 \right]^{-1/4}, \quad (16)$$

where the dimensionless form of the bed shear stress, Shields parameter θ , is given by

$$\theta = \frac{U_f^2}{(s-1)gd}. \quad (17)$$

2.3. Hydrodynamic, morphological, and soil models

The numerical model used in this study integrates the fully coupled hydrodynamic and morphological CFD framework introduced by Jacobsen (2011), Jacobsen et al. (2014), with the additional incorporation of the dynamic seepage response obtained by the anisotropic Biot's consolidation model (Biot, 1941).

The hydrodynamic model solves the incompressible three-dimensional RANS equations within a Cartesian coordinate system. The closure is achieved using the two-equation $k-\omega$ turbulence model proposed by Wilcox (2006, 2008), where k represents turbulent kinetic energy, and ω denotes specific turbulent dissipation rate. The morphological model addresses both bed load and suspended load transport. Bed load transport follows the method described in Sections 2.1 and 2.2. Expressions for critical bed shear stress and bed load transport are adapted to incorporate the influence of three-dimensional seepage forces and bed-slope modifications. The suspended sediment model is based on a turbulent-diffusion equation (Fredsøe and Deigaard, 1992, p. 238). The evolution of seabed morphology, represented by bed elevation, is governed by a sediment continuity (Exner) equation. A physics-based sand slide model (Roulund et al., 2005) is employed to ensure that the local bed angle does not surpass the angle of repose. The evolution of bed morphology is based on the instantaneous sediment transport fields. Note that the model does not rely on averaged morphological rates over a specific time frame or any other temporal scale. Therefore, morphological and hydrodynamic times are equivalent, i.e., the morphological and hydrodynamic models are fully coupled. For comprehensive understanding, readers are directed to Fuhrman et al. (2014) for further elucidation. The seepage response is based on the soil model developed by Li et al. (2020c) who employed the classical Biot's consolidation equations (Biot, 1941) to simulate the interaction between the soil skeleton and the pore fluids, considering the anisotropic soil characteristics. The soil domain is governed by a quasi-static momentum balance equation for soil mixture and a mass balance equation of the pore fluid based on Darcy's law. The seabed is nearly saturated, and the soil skeleton generally obeys Hooke's law with elastic properties. The governing equations and the solving procedure for this soil model can be referred to Li et al. (2020c).

Fig. 2 shows the sketch and flowchart of the coupled CFD model. At each time step, the tsunami wave signal prescribes the dynamic wave pressure on the fluid–soil interface to calculate the pore pressures and

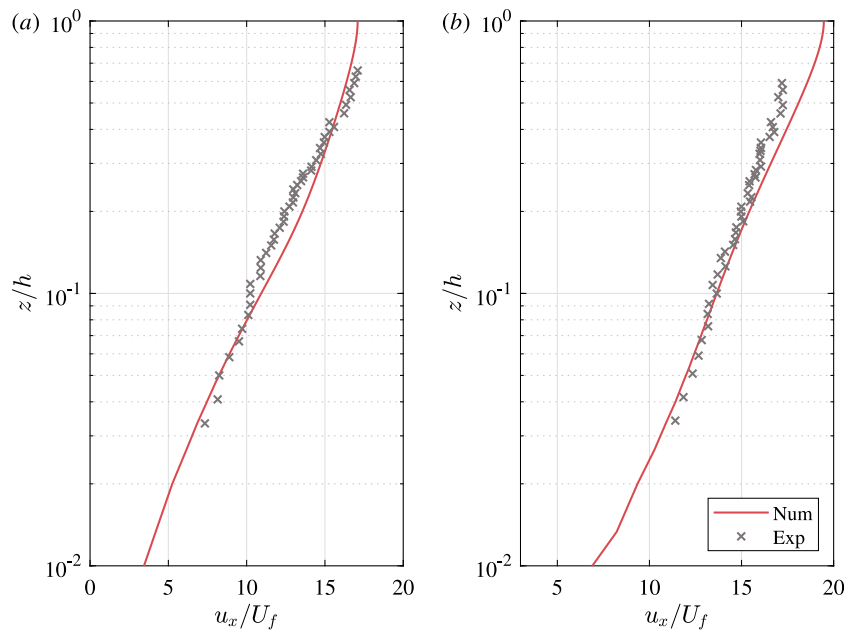


Fig. 3. Comparison of velocity profiles of the streamwise flow subjected to the seabed (a) suction and (b) injection between the numerical and experimental results.

displacements in the soil domain. The pore-pressure gradients are then obtained at the surficial seabed and transferred to the hydrodynamic and morphological modules. The seepage velocities are specified at the seabed surface, which influences the boundary layer and the resulting bed shear stress. Moreover, the seepage forces alter the critical Shields parameter and the bed load transportation. The flow drives the transport of bed and suspended loads, leading to the evolving bed elevation. The underneath bed, in turn, updates the bottom boundary topography by moving the computational mesh, influencing the fluid dynamics. The fully coupled model is solved using the open-source CFD toolbox OpenFOAM, version foam-extend 3.1. Employing a finite volume spatial discretization with a collocated variable arrangement, it is coupled with a standard PIMPLE algorithm (Patankar and Spalding, 1972; Issa, 1986).

2.4. Model validations

2.4.1. Velocity profile subjected to the bottom seepage

First, we validate the present model against the experiment conducted by Dey and Nath (2010) for the velocity profiles of a turbulent open-channel flow over an immobile rough bed subjected to boundary injection and suction. The experiment was conducted in a glass-walled rectangular flume. The rough bed placed in the flume is simulated by a uniform gravel layer with a median diameter $d = 4.1$ mm and a specific gravity $s = 2.65$. The gravel bed has a roughness length k_s of d based on velocity measurements, as reported by Dey and Nath (2010). Under bed injection and suction conditions, the seepage kit beneath the gravel layer produces uniformly distributed seepage with velocities $v_s = 4$ mm/s and $v_s = -3$ mm/s, respectively. The water depth h and the friction velocity U_f for the streamwise flow without the seepage are 0.15 m and 0.033 m/s, respectively. In the present computational flume for numerical reproduction, the smallest cells near the bed have a height equal to $0.5d$. The flow is driven by the body force $F = U_f^2/h$ and eventually reaches a fully developed state with a separate 1DV boundary layer simulation. Thereafter, the profiles of u , k , and ω are specified at the inlet boundary of the two-dimensional simulation based on a Dirichlet boundary condition. The seepage velocity is then applied at the bottom boundary of the numerical flume. Fig. 3 compares the velocity profiles of the streamwise flow, u_x , subjected to the seepage between the numerical results and the experimental data measured at

the center line of the flume. It is seen that a good agreement is achieved for both injection and suction conditions, especially for the water layer near the bed. The discrepancies near the water surface might be due to the free surface effects as the Froude number based on the water depth $Fr \sim O(0.5)$, see Roulund et al. (2005).

2.4.2. Tsunami-induced scour around a monopile

Section 2.4.1 has validated the capability of the present model to simulate the velocity profile of the turbulent boundary layer subjected to the bottom seepage. To further validate the capability of tsunami scour modeling, the laboratory experiment of Larsen et al. (2018) on the tsunami-induced scour around a monopile is numerically reproduced herein. Note that this experiment did not include seepage effects, since a pump is used to generate the flow without considering the varying wave surface. Therefore, in our simulation of this experiment, the seepage effect is excluded as well. In the physical experiment, the down-scaled tsunami is represented as a single (elongated soliton) wave with the free-stream velocity of $U_x = U_m \operatorname{sech}^2\left(\frac{2\pi}{T}t\right)$ in a water depth $h = 2.7D$, where the circular pile diameter $D = 0.1$ m. The median diameter of the sandy bed $d = 0.18$ mm and the grain Reynolds number $U_f d/v \approx 3$ as reported by Larsen et al. (2018), where U_f is the friction velocity and v is the kinematic viscosity. The critical Shields parameter $\theta_{co} = 0.06$ is then used according to the classic Shields diagram with the curve fitting equation proposed by Sui et al. (2021). The present numerical simulation applies the same velocity signal as that in the experiment of Larsen et al. (2018), i.e., a single wave. Note that Larsen et al. (2018) also numerically reproduced the experiment in their work, with different input parameters compared to the present study. The critical Shields parameter they adopted, 0.05, is slightly smaller than the reality, as mentioned by Larsen et al. (2018). Therefore, we will only compare with their experimental results here, as a direct comparison to their numerical results is not feasible.

Fig. 4(a) shows the velocity profiles for the streamwise flow at the peak with the maximum free-stream velocity $U_m = 0.51$ m/s and the characteristic wave period $T = 123$ s. The present numerical model effectively reproduces the dynamics of the transient boundary layer. Notably, the boundary layer induced by the tsunami does not extend across the entire water depth (Williams and Fuhrman, 2016; Larsen and Fuhrman, 2019b). The experimental case with $U_m = 0.42$ m/s and $T = 147$ s was selected for tsunami scour validations. Fig. 4(b)

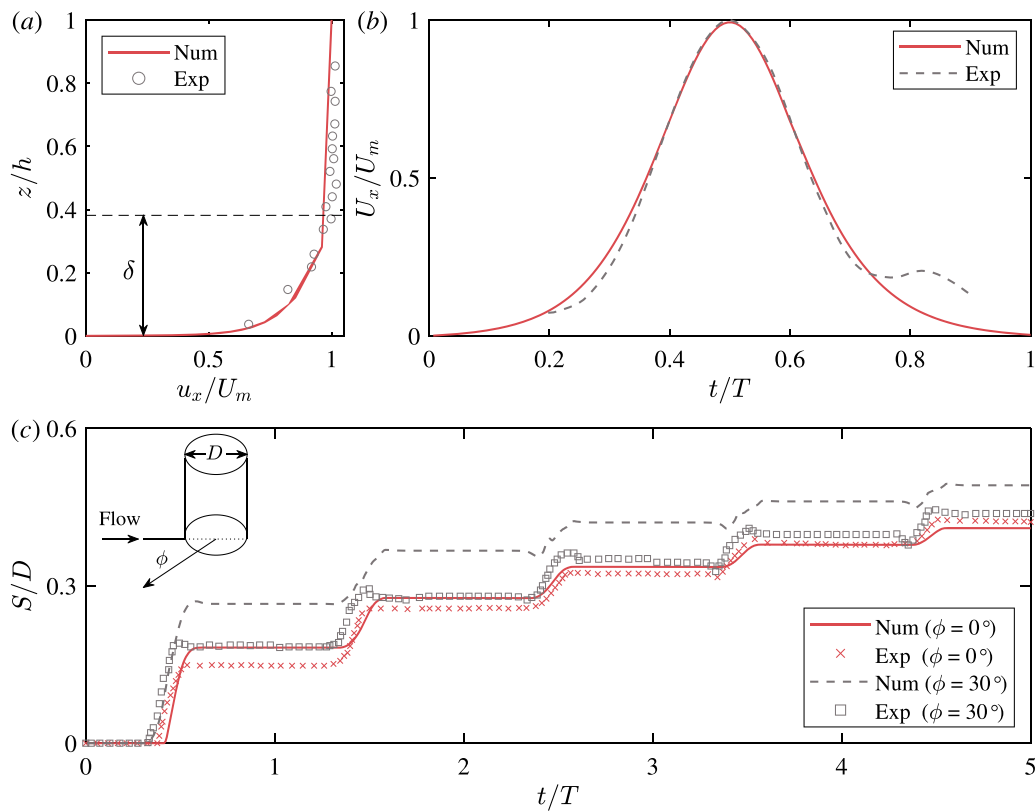


Fig. 4. Comparison of (a) velocity profile at the peak, (b) free-stream velocity, and (c) scour depth at the front ($\phi = 0^\circ$) and front side ($\phi = 30^\circ$) of a circular pile between the numerical and experimental results.

compares the free-stream velocity between the experimental and numerical results. The flow velocity in the numerical flume is generally consistent with the experimental measurement of Larsen et al. (2018). Some discrepancies are observed around the initial acceleration and final deceleration phases due to the difficulties in controlling the pump to fit the sech^2 profile in the experiment (Larsen et al., 2018). Fig. 4(c) presents the development of scour depth at the front ($\phi = 0^\circ$) and front side ($\phi = 30^\circ$) of the circular pile, where ϕ is the angle from the center line. After several waves in succession, the predicted scour depth gradually develops in a cumulative way, which reasonably agrees with the experimental measurement, especially for $\phi = 0^\circ$. Note that the scour depth at the front side of the pile is remarkably overestimated, particularly during the first tsunami period. This is because the bed in the experiment is not completely flat as in the computational domain, although it is leveled case by case, as reported by Larsen et al. (2018). The small bed forms can increase the flow resistance and thus decrease the bed shear stress compared with the model prediction (Larsen et al., 2018). This influence fades away after several tsunami waves as the scour depth is expected to approach equilibrium.

Overall, the above validations against the laboratory experiments demonstrate the numerical model's capability to reliably predict the tsunami-induced scour around a circular pile considering seepage effects.

2.5. Model setup and boundary conditions

Unless otherwise stated, the fluid computational domain has a length of $20D$, a width of $15D$, and a height of $2.7D$, as sketched in Fig. 5, where D is the diameter of the circular pile. The pile fixed in the center of the domain is set as the origin ($x = 0$ and $y = 0$). The computational domain is spatially discretized into finite volumes with varying sizes, where the heights of the cells closest to the pile and seabed are $0.02D$ and d , respectively, same as Larsen

et al. (2017). The number of nonuniform cells along the x , y , and z directions are 116, 96, and 48, respectively. Accordingly, the total number of cells comprising the computational mesh is 340992. The maximum Courant number is set to 0.35. During the scour calculations, the computational mesh is continuously deformed according to the evolution of seabed topography. To avoid excessive erosion caused by the flow at the boundary, the seabed is constrained near the inlet and outlet boundaries and gradually relaxed to its full morphology, i.e., the seabed topography near the inlet and outlet boundaries is fixed without mesh deformation (Baykal et al., 2015, 2017; Larsen et al., 2017, 2018). The soil computational domain has the same length and width as the fluid domain and a thickness of $5.6D$, where the heights of the cells closest to the pile and seabed are 0.02 D .

Boundary conditions for all upcoming simulations are as follows. In the fluid domain, the top of the computational domain (Fig. 5) is modeled as a frictionless slip wall, where the normal velocity component is set to zero, and the tangential component of velocity and scalar hydrodynamic quantities have a zero normal gradient. It means that we perform single-phase fluid simulations, i.e., the free surface of tsunami waves is not involved in this study. It is reasonable, provided that the Froude number based on the water depth (h), Fr , is sufficiently low (Roulund et al., 2005). $Fr = U_m/\sqrt{gh} = O(0.18)$ for the simulated tsunami waves shows negligible free surface effects, where U_m is the velocity magnitude and g is the gravitational acceleration. For the side boundaries, a slip boundary condition is applied for the velocity u , and a zero-gradient boundary condition is imposed for other quantities. It is noted that the more complex topography (e.g., run-up on a beach) and presence of structures are expected to affect the sinusoidal velocity signal (Hu et al., 2023; Hu and Li, 2023). However, modeling the free surface of the three-dimensional (3D) full-scale tsunami-scour problem gives expensive computational costs with the advanced CFD models herein, thus we focus only on the sediment transport process within the boundary layer. In our 3D simulations, tsunami waves are generated based on a Dirichlet condition at the inlet boundary for the simulations

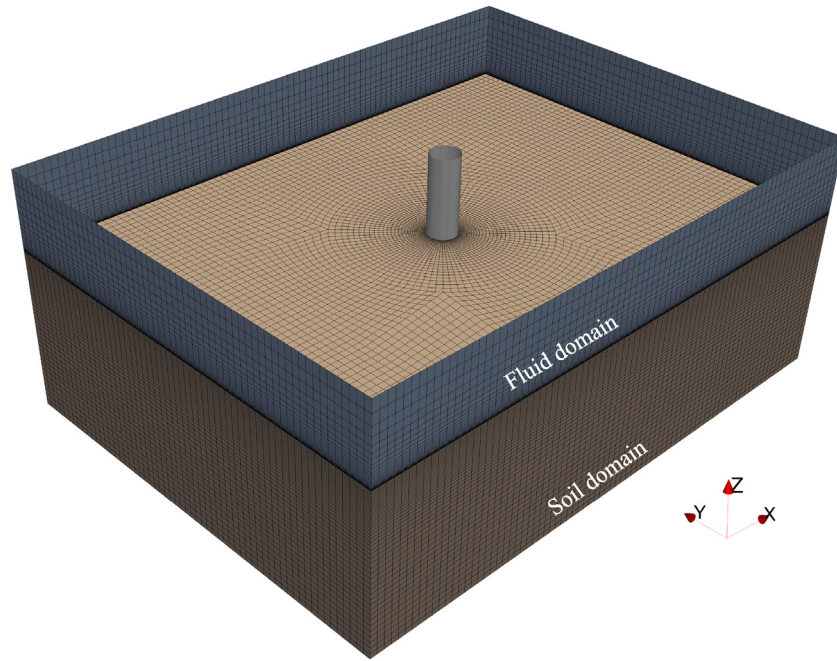


Fig. 5. Computational domains.

with the pile. The profiles of u , k , and ω are derived from a separate simulation that models a 1DV pure boundary layer in the same domain but without the pile, the same as that in Li et al. (2020b). Neumann boundary conditions are enforced for the other variables, while zero-gradient boundary conditions are set at the outlet boundary, except for the pressure p , which is specified as zero.

The pile and seabed boundaries are modeled as no-slip hydraulically smooth and rough walls, employing a generalized wall function approach. The friction velocity U_f is computed from the tangential velocity at the nearest cell center, following the profile formulated by Cebeci and Chang (1978), which extends the work of Van Driest (1956) to account for roughness effects. At the seabed, Nikuradse's equivalent sand grain roughness is set as $k_s = 2.5d$ to represent hydraulic roughness, where d denotes the median diameter of the particle. For the pile surface, a minimal value of $k_s = 1 \times 10^{-5}$ m is applied to signify hydraulically smooth conditions. The friction velocity is subsequently employed for k and ω computations in cells adjacent to the wall. Additional details can be found in Fuhrman et al. (2014). According to Darcy's law, the seepage velocity $v_s = Ki$ is prescribed at the bottom seabed boundary, including the kinematic effect of seepage flows, where K is the soil permeability.

At the wave-seabed interface within the soil domain, a zero-traction condition is applied to the soil, while the pore pressure is set to the dynamic wave pressure using a Dirichlet boundary condition. At the pile-soil interface, a zero-gradient boundary condition is imposed on the pore pressure, and soil displacement is constrained to zero, assuming the pile is immovable. Along the lateral boundaries of the soil, the pore pressure is assigned a zero normal gradient, and the soil skeleton is allowed to slip. At the bottom boundary of the soil, a zero-gradient condition is maintained for pore pressure, and the soil skeleton is fixed with zero displacement.

3. Tsunami signal and seepage response

We use the advanced CFD models to investigate the full-scale tsunami scour with three-dimensional seepage effects. The parameters of the tsunami wave, seabed, and pile are listed in Table 1. The renowned signal of the 2004 Indian Ocean tsunami event, as recorded aboard the yacht Mercator at a water depth of $h = 14$ m, serves as the

field tsunami scale in this study. Madsen et al. (2008) approximated the leading wave of this signal as a sinusoidal wave characterized by an amplitude $A_w = 2.5$ m and a period $T = 780$ s. The two half-cycles can be considered as an elevation wave and depression wave (Larsen et al., 2017), respectively. Thus, the velocity can be obtained by linear shallow water theory, i.e., $U_m = A_w \sqrt{g/h}$. The wave pressure distribution is generally assumed to vary hydrostatically under long waves in shallow water. The dynamic wave pressure on the seabed varies linearly with the free surface elevation $p = \rho g A_w \sin(\frac{2\pi}{T}t)$. A sinusoidal model provides a more accurate representation of this tsunami event than a solitary wave model which only accounts for positive surface displacements and does not allow for the independent determination of effective period and amplitude, as discussed by Madsen et al. (2008). Moreover, based on free surface wave records from multiple locations during the 2011 Tohoku tsunami in Japan, Chan and Liu (2012) similarly concluded that the leading tsunami waves, both in the near-field and far-field regions, can be described as small-amplitude long waves, aligning with the used linear shallow-water theory (Larsen et al., 2017). The boundary layer thickness δ is estimated by the expression given by Williams and Fuhrman (2016) for the hydraulically rough condition:

$$\frac{\delta}{a} = 0.05 \left(\frac{a}{k_s} \right)^{-0.11}, \quad (18)$$

where $a = U_m T / 2\pi$ is the characteristic length scale. The Keulegan-Carpenter number (Keulegan and Carpenter, 1958) is given by

$$KC = \frac{U_m T}{D}, \quad (19)$$

which govern the formation and excursion of the wake pattern during oscillatory motion. As tsunami waves propagate, the pore pressure p_e in the underlying soil bed is estimated by the anisotropic soil model driven by the dynamic wave pressure. The hydraulic gradient of seepage flows $i = (\partial p_e / \partial x, \partial p_e / \partial y, \partial p_e / \partial z) / \rho g$ at the surficial seabed is then obtained and imposed on the seabed of the hydrodynamic and morphological modules at each time step. In our simulations, each full-scale tsunami period requires approximately 20 days of computation using 36 processors on the supercomputer of the National Supercomputing Centre (NSCC), Singapore.

Fig. 6 presents the calculated pore-pressure profiles and the hydraulic gradients for the full-scale tsunami. The downward pressure

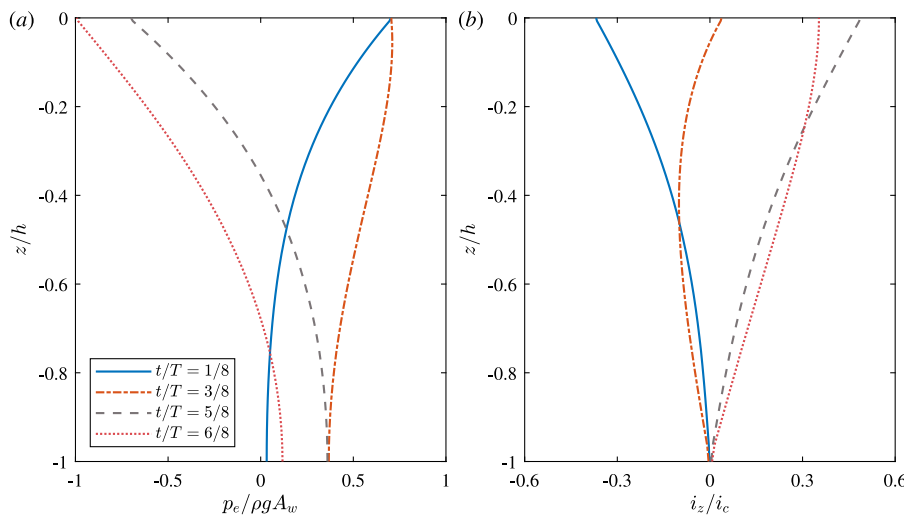


Fig. 6. Tsunami-induced (a) pore-pressure head profiles and (b) vertical hydraulic gradient i_z profiles at the front of the pile.

Table 1

Parameters of the tsunami wave, seabed, and pile.

Parameters	Value	Unit
Tsunami parameters		
Wave amplitude (A_m)	2.5	[m]
Wave period (T)	780	[s]
Water depth (h)	14	[m]
Boundary layer thickness (δ)	3.25	[m]
Froude number (Fr)	0.18	[–]
Keulegan–Carpenter number (KC)	653	[–]
Reynolds number (Re)	5.2×10^6	[–]
Seabed parameters		
Sediment median diameter (d)	0.35	[mm]
Seabed thickness (h_s)	14	[m]
Permeability (K)	1×10^{-3}	[m/s]
Shear modulus (G_s)	2.64×10^7	[N/m ²]
Specific gravity (s)	2.65	[–]
Poisson's ratio (ν)	0.3	[–]
Saturation factor (S_r)	0.9	[–]
Porosity (n)	0.4	[–]
Pile parameters		
Diameter (D)	2.5	[m]

force can be observed during the elevation wave, while the upward pressure force is exerted on the upper soil during the depression wave. Fig. 7(a) presents the free-stream velocity during the tsunami propagation on a fixed flatbed. The corresponding surficial seepage response at the front of the circular pile is sequentially suction (flow into the bed) and injection (flow out of the bed). The x - and y -directed hydraulic gradients are negligible compared with the vertical direction. Fig. 7(b) shows the tsunami-induced Shields parameter θ_o (Eq. (17)) and critical Shields parameter θ_{co} (Eq. (5)) at the flatbed. The “seepage-on” case considers the seepage response induced by the tsunami loading in the underlying soil. The “seepage-off” case is a control group without considering the seepage. Compared with the “seepage-off” case, the seabed suction increases both the bed shear stress (θ_o) and critical bed shear stress (θ_{co}). However, the seabed injection shows the opposite effect. The competing trends of the fluid–sediment momentum transfer and onset threshold of sediment motion influence the tsunami-induced sediment (Hu et al., 2024).

4. Seepage effects on tsunami flow features around a circular pile

In this section, we conduct full-scale rigid-bed simulations to investigate the effects of dynamic seepage response on main flow characteristics around a vertical slender pile subjected to tsunamis, i.e., separate

horseshoe vortices formed in front and back of the pile during successive half cycles, lee-side vortices in the form of vortex shedding, and contracted streamlines around the side edges of the pile (Sumer and Fredsøe, 2002, pp. 150–151).

4.1. Horseshoe vortex

The horseshoe vortex around a circular pile exposed to flow can tremendously amplify the bed shear stress relative to its undisturbed value (Baker, 1979; Hjorth, 1975; Roulund et al., 2005; Baykal et al., 2017), which mainly influences the scouring processes. The horseshoe vortex is induced by the combined action of approach flow rotation and adverse pressure gradient caused by the presence of the pile (Sumer and Fredsøe, 2002). The boundary layer separates and forms a spiral vortex around the pile, trailing off downstream. The size of the horseshoe vortex in front of a circular pile in the context of waves is mainly determined by three factors: the ratio of bed boundary layer thickness to the pile diameter δ/D ; the ratio of bed roughness to the pile diameter k_s/D ; and Keulegan–Carpenter number KC (Baker, 1979; Sumer and Fredsøe, 2002). Due to the large KC number of the simulated tsunami waves in the present study (see Table 1), the wave excursion is large enough that the flow during each half cycle resembles a steady current. Consequently, the horseshoe vortex beneath tsunamis is expected to behave similarly to that in a current (Larsen et al., 2017, 2018).

Fig. 8 displays the instantaneous vortical structures represented by the Q iso-surfaces around the pile with and without considering the seepage effects, identified by the so-called Q -criterion (Hunt et al., 1988). The Q -criterion identifies a vortex as a coherent fluid region exhibiting a positive second invariant ($Q > 0$) of the velocity gradient tensor:

$$Q = \frac{1}{2} \left(|\Omega_{ij}|^2 - |S_{ij}|^2 \right) > 0 \quad (20)$$

that is the region where the magnitude of the mean rotation tensor Ω_{ij} prevails over the magnitude of the strain-rate tensor S_{ij} , where

$$\Omega_{ij} = \frac{1}{2} \left(\frac{\partial u_i}{\partial x_j} - \frac{\partial u_j}{\partial x_i} \right), S_{ij} = \frac{1}{2} \left(\frac{\partial u_i}{\partial x_j} + \frac{\partial u_j}{\partial x_i} \right). \quad (21)$$

As shown in Fig. 8(a,b), the free-stream flow is from left to right and reaches the peak velocity at $t/T = 0.25$. The horseshoe vortex in front of the circular pile and lee-wake shed vortices at the back are observed in the flow visualization. In the presence of the seabed suction, the size of the horseshoe vortex barely decreases compared to that of the impermeable bed. In Fig. 8(c,d), the free-stream flow reverses and peaks at $t/T = 0.75$. The size of the horseshoe vortex with the seabed injection marginally increases compared to that without considering

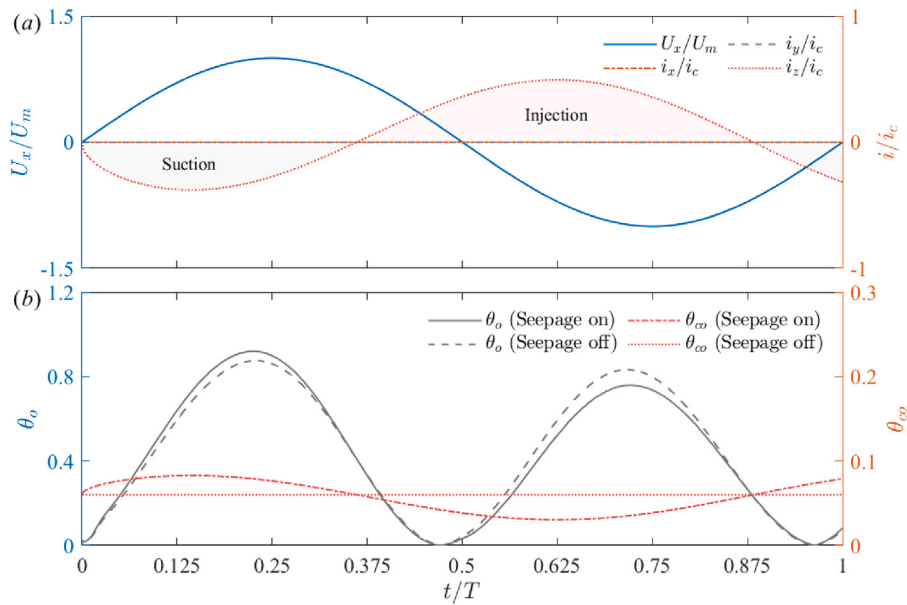


Fig. 7. Tsunami-induced (a) free-stream velocity and corresponding surficial hydraulic gradient at the front of the pile, (b) Shields parameter, and critical Shields parameter at the flatbed.

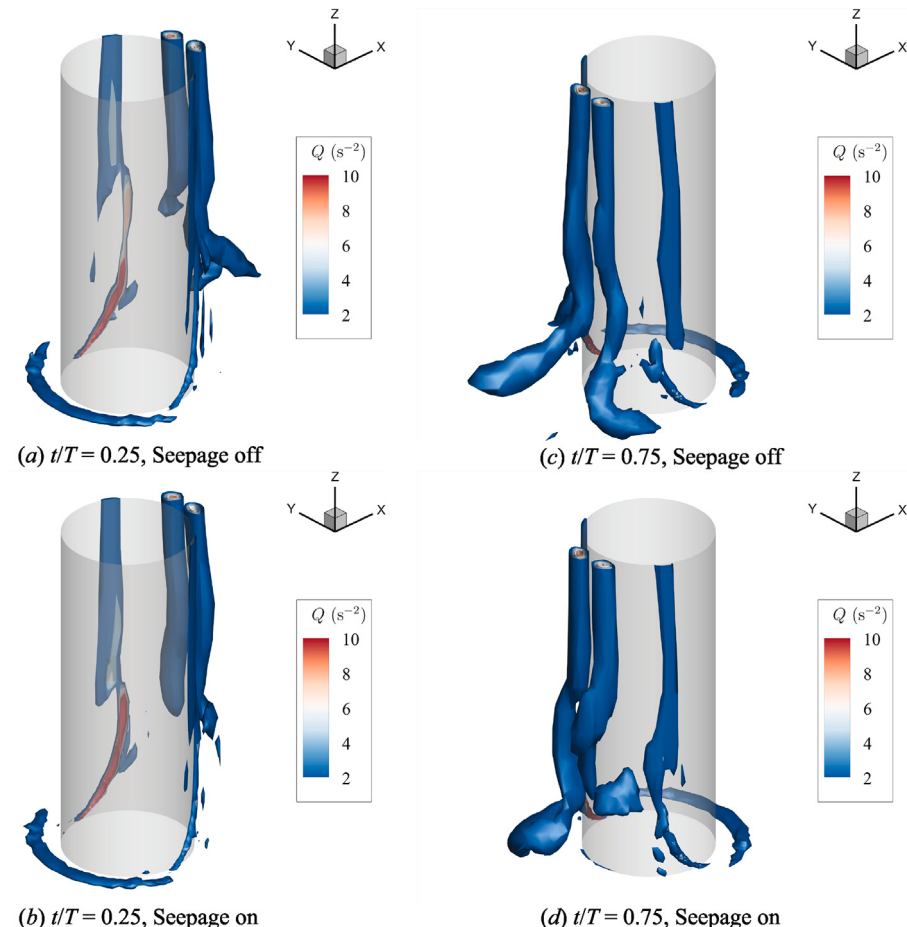


Fig. 8. Q representations for the horseshoe vortex and the shed vortices around the circular pile at $t/T = 0.25$ and $t/T = 0.75$ (a,c) without and (b,d) with considering the seepage effects.

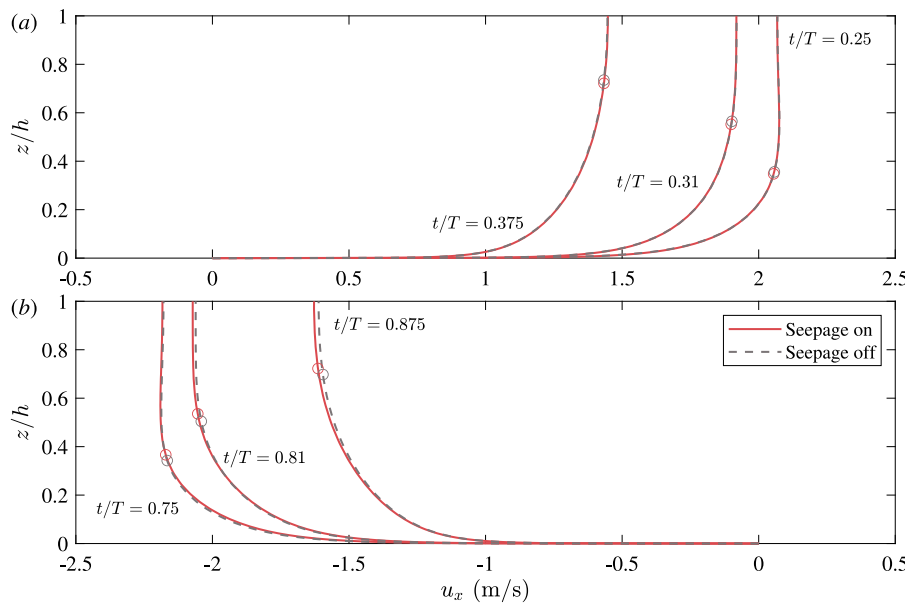


Fig. 9. Velocity profiles at different times during the (a) elevation and (b) depression with and without considering the seepage effects, where (o) marks the boundary layer thickness.

the seepage effects. These trends will be more clearly shown in the characteristic length x_s of the horseshoe vortex depicted in Fig. 10 and the upward-directed pressure gradient inside the horseshoe vortex illustrated in Fig. 11. The decrease/increase in the size of the horseshoe vortex is because of the decrease/increase of boundary layer thickness caused by the seabed suction/injection, as shown in Fig. 9. The variations in the boundary layer thickness are more pronounced with the seabed injection during the depression wave. The separation of the seabed boundary layer will be delayed if the ratio of boundary layer thickness to the pile diameter δ/D decreases (Baker, 1979; Sumer et al., 1997; Sumer and Fredsøe, 2002, pp. 153–154), presumably leading to a smaller-size horseshoe vortex. The visible lee-side vortices will be discussed in Section 4.2.

Fig. 10(a) shows the variation of bed shear stress amplification τ/τ_o along the x -axis at the horseshoe vortex side of the circular pile, where τ is the local bed shear stress and τ_o is the undisturbed bed shear stress in the far velocity field. The negative τ/τ_o represents the position of the horseshoe vortex in the streamwise direction at the incoming flow side. The distance x_s from the zero-crossing of the bed shear stress to the pile center is defined as the length that characterizes the size of the horseshoe vortex. At $t/T = 0.25$ ($x/D < 0$ in front of the pile), the seabed suction barely decreases x_s and τ/τ_o , as compared to the impermeable seabed. At $t/T = 0.75$ ($x/D > 0$ at the back of the pile), the seabed injection marginally increases the size of the horseshoe vortex and the amplification of bed shear stress within it. Note that the bed shear stress inside the horseshoe vortex might be under-predicted as the coherent structures can be damped or smoothed by the RANS simulations (Baykal et al., 2017).

Fig. 11 illustrates the vertical pressure gradient $-\partial(p/\rho)/\partial z$ fields in $y-z$ planes at $x = x_r$ (left panels) and $x = x_d$ (right panels) given in Fig. 10(a). The upper downward-directed pressure gradient (negative $-\partial(p/\rho)/\partial z$ values) causes the downflow due to the deceleration of the approach flow. The upward-directed pressure gradient (positive $-\partial(p/\rho)/\partial z$ values) on the seabed corresponds to the position of the horseshoe vortex in the vertical direction. The upward-directed pressure gradient can drive sediment suspension via upward vertical flow (Baykal et al., 2015). In Fig. 11(a,b), the upward-directed pressure gradient with the seabed suction is marginally less pronounced than that without considering the seepage effects. This, combined with the increased onset threshold of sediment transport shown in Fig. 7(b), can marginally reduce the scour at the front of the circular pile during

the elevation wave. More details will be shown in Section 5.1. In Fig. 11(c,d), the seabed injection yields a marginally greater area and magnitude of the upward-directed pressure gradient than that without considering the seepage effects. The differences in the instantaneous $-\partial(p/\rho)/\partial z$ field between $x = x_d$ and $x = x_r$ is due to the slight phase shift between the boundary layer and the free-stream flows, which also can be seen between θ_o and U_x in Fig. 7(a,b). Overall, the seepage response shows insignificant effects on the size and intensity of the horseshoe vortex in front and back of the circular pile.

4.2. Streamline contraction and lee-wake vortices

Fig. 10(b) depicts the amplification of bed shear stress τ/τ_o along the y -axis near the side edges of the circular pile. The contraction of the streamlines essentially determines the amplification of the positive bed shear stress. The maximum τ/τ_o is reduced by 8% due to the seabed suction, while it is increased to $O(4)$ since τ_o with the seabed injection decreases more obviously as shown in Fig. 7(b). The variations of the bed shear stress caused by the seepage response can potentially influence the sediment transport near the side edges of the circular pile, which will be shown in Section 5.1. Note that the span with amplified bed shear stress ($\tau/\tau_o > 1$) is very similar between the “seepage-on” and “seepage-off” cases regardless of the seepage direction.

We then investigate the seepage effects on the lee-wake vortices of the circular pile in tsunami waves. The formation of lee-wake vortices is primarily caused by the rotation within the boundary layer over the surface of a pile. The shear layers that originate from the side edges of the pile roll up and create these vortices in the lee wake of the pile (Sumer and Fredsøe, 2002; Baykal et al., 2017). The Reynolds number $Re = U_m D / \nu$ of present tsunami waves is 5.2×10^6 , which implies that the vortex shedding occurs in the turbulent regime (Sumer, 2006). Fig. 8 illustrates that the vortex shedding occurs in a two-cell regime over the height of the pile, as the velocity profiles of the approach flow are not uniform from the seabed to the upper water column. The two-cell regime refers to the vortical structures breaking into two parts along the pile; one moves slowly close to the seabed, while the upper rest resembles the lee-wake vortices of a free cylinder (Baykal et al., 2015). The lee-wake vortices of a circular pile in tsunami waves behave both current-like due to the existence of the two-cell vortical structures (Baykal et al., 2015) and wave-like due to the insignificant

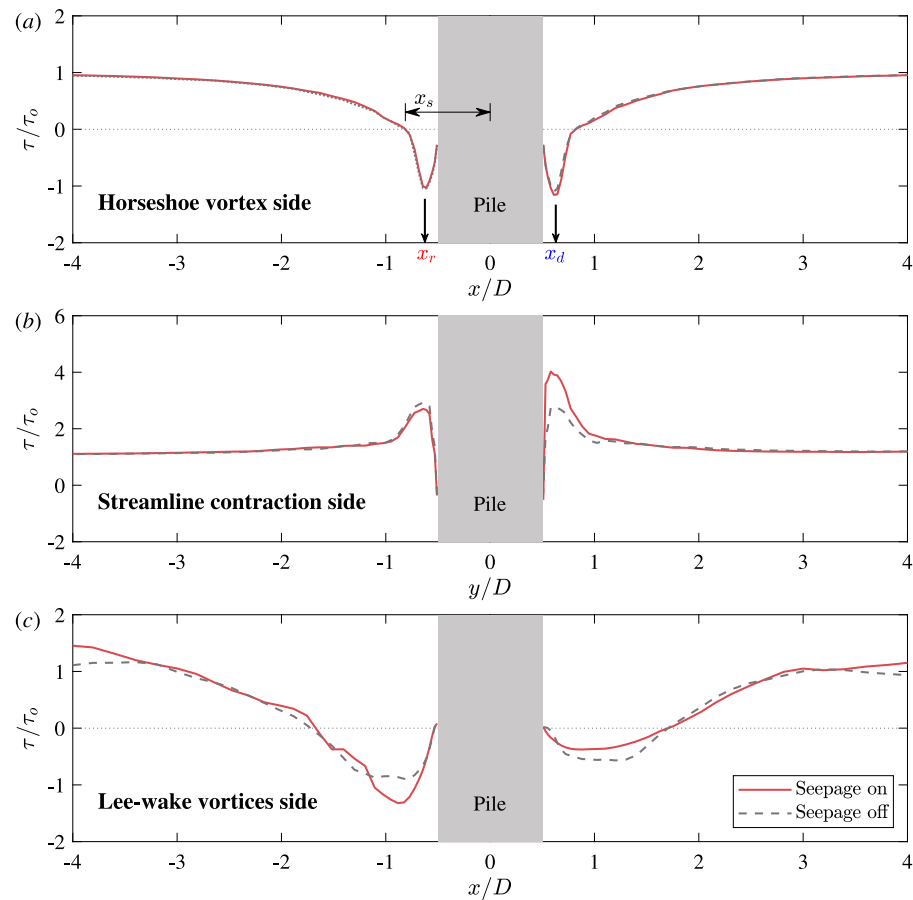


Fig. 10. Amplification of bed shear stress along the x -axis at the (a) horseshoe vortex side (at $t/T = 0.25$ for $x/D < 0$ and $t/T = 0.75$ for $x/D > 0$), (b) streamline contraction side (at $t/T = 0.25$ for $y/D < 0$ and $t/T = 0.75$ for $y/D > 0$), and (c) lee-wake vortices side (at $t/T = 0.75$ for $x/D < 0$ and $t/T = 0.25$ for $x/D > 0$) of the circular pile.

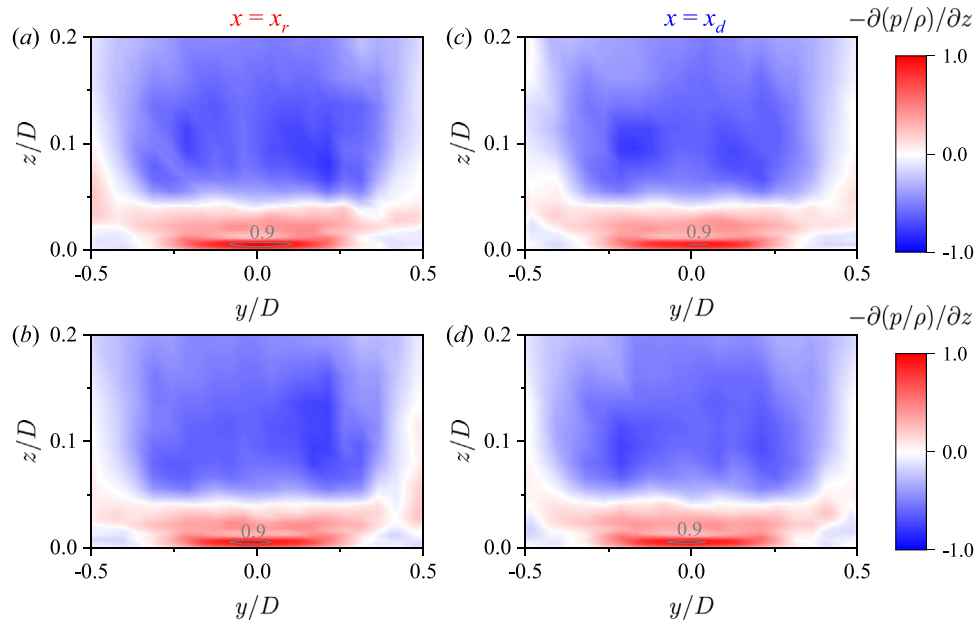


Fig. 11. Vertical pressure gradient fields at the longitudinal sections (y - z planes) given in Fig. 10(a) for the seabed (a,c) without and (b,d) with considering the seepage effects.

counter-rotating vortices near the seabed (Baykal et al., 2017). The two-cell vortical structures are more visible in the side view of the position of boundary layer separation in Fig. 12, where the streamwise velocity reverses along the vertical pile. The lower cell extends up to $z/D = 1.0$

from the seabed, similar to that in a steady current studied by Baykal et al. (2015). At $t/T = 0.25$ ($x/D > 0$ at the lee side of the pile), the effect of seabed suction on the boundary layer separation is minimal. At $t/T = 0.75$ ($x/D < 0$ in front of the pile), the seabed injection slightly

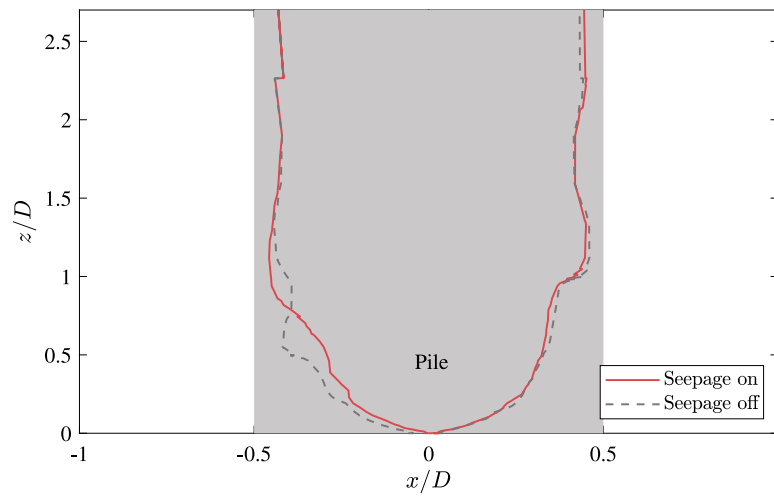


Fig. 12. Position of boundary layer separation (at $t/T = 0.75$ for $x/D < 0$ and $t/T = 0.25$ for $x/D > 0$) over the height of the pile.

advances the boundary layer separation. The thickness of the tsunami boundary layer experiencing seabed injection increases, as shown in Fig. 9, reducing momentum exchange between the outer flow and the hydraulically rough seabed. Consequently, the decreased streamwise momentum in the boundary layer leads to earlier separation.

Fig. 10(c) depicts the bed shear stress amplification along the x -axis at the lee-wake vortices side of the circular pile. In the absence of seepage response, the amplification in the bed shear stress concerning its undisturbed value can be $O(0.7)$ during the tsunami propagation. At $t/T = 0.25$ ($x/D > 0$), the bed shear stress amplification τ/τ_o underneath the lee-wake vortices generally decreases when considering the seabed suction. At $t/T = 0.75$ ($x/D < 0$), τ/τ_o shows an opposite trend in the presence of seabed injection. The abovementioned variations of boundary layer separation position over the pile cause the seepage effects to extend to a few pile diameters at the lee-wake vortices side. Overall, the seepage response to tsunami loading exhibits more obvious effects on the amplification of bed shear stress at the streamline contraction and lee-wake vortices sides than the horseshoe vortex side.

4.3. Amplification of bed shear stress

The amplification of bed shear stress along the x - and y -axes has been discussed for the horseshoe vortex side in Section 4.1 and for the streamline contraction and lee-wake vortices sides in Section 4.2. This section illustrates the overall picture of bed shear stress amplification around the pile with and without considering seepage effects, as shown in Fig. 13, where the amplification of bed shear stress herein is the ratio of the maximum magnitude of the bed shear stress vector to the undisturbed bed shear stress $|\tau_{max}|/\tau_{o,max}$.

In Fig. 13(a), the maximum amplification in bed shear stress appears at the front side ($\phi \approx 60^\circ$) of the pile. In the absence of seepage flows, the bed shear stress can be as much as a factor of 6 larger than the undisturbed bed shear stress, which falls between $O(3-4)$ in wind-generated waves and $O(10)$ in a steady current (Sumer et al., 1997; Sumer and Fredsøe, 2002; Baykal et al., 2015, 2017). The maximum amplification is mainly determined by the combined effect of the horseshoe vortex and the contraction of streamlines, which is similar to but less significant than that of a steady current in Sumer and Fredsøe (2002). The amplification fields are almost symmetric as the tsunami signal is sinusoidal. The seepage response leads to the asymmetric $|\tau_{max}|/\tau_{o,max}$, as shown in Fig. 13(b). This is mainly due to the variations of $\tau_{o,max}$ in the far field. The maximum amplification decreases at the front side of the pile, while it increases to $O(8)$ at the back side ($\phi \approx 120^\circ$). The increase in amplification can naturally induce a rapid scour

near this region, combined with the decrease in the onset threshold of sediment transport caused by the seabed injection shown in Fig. 7(b). The stronger tsunami scour with the seabed injection will be shown in Section 5.1.

Overall, the amplification of bed shear stress during tsunami propagation is intermediate between wind-generated waves and a steady current. The seepage response to tsunami loading yields a notable difference in the amplification between the elevation and depression. Specifically, the seabed injection during the depression wave primarily governs the maximum amplification.

5. Seepage effects on tsunami-induced scour around a circular pile

In this section, we investigate the effects of seepage response on tsunami-induced scour around a circular pile by enabling the seabed morphological evolution in the present fully coupled CFD model. In Section 5.1, the evolution of the scour depth and seabed topography is compared between cases with and without considering the seepage effects during the tsunami propagation. In Section 5.2, we present the seepage effects on sediment transport rate to elaborate the tsunami scour mechanisms.

5.1. Tsunami scour evolution

Fig. 14 shows the temporal variation of the scour depth S/D at different pile positions during the tsunami propagation. In Fig. 14(a) at the front ($\phi = 0^\circ$) of the pile, the scour hole gradually deepens and then reaches a temporary equilibrium stage around $t/T = 0.375$. The seabed suction marginally reduces the temporary equilibrium scour depth. This is mainly because of the increased onset threshold of sediment transport as shown in Fig. 7(b). After the flow reversal, the scour depth with and without the seepage effects tends to be indistinguishable. In Fig. 14(b) at the side ($\phi = 90^\circ$) of the pile, the scour depth starts to grow more slowly from the peak seabed suction intensity, compared to the impermeable bed. The temporary equilibrium scour depth is slightly reduced by 10%, which is primarily owing to the combination of the lower bed shear stress amplification underneath the contraction of streamlines as shown in Fig. 10(b) and the increased critical Shields parameter as shown in Fig. 7(b). During the depression wave, the scour hole experiences a rapid backfilling, followed by further erosion in the reversed flow. It is observed that the final scour depth after one tsunami wave cycle is lower when considering the seepage response. This is owing to the more deposition emanating from the stronger scour at the back ($\phi = 180^\circ$) of the pile, as shown in Fig. 14(c). Specifically, the rapid scour occurs at the end of the depression wave, when the

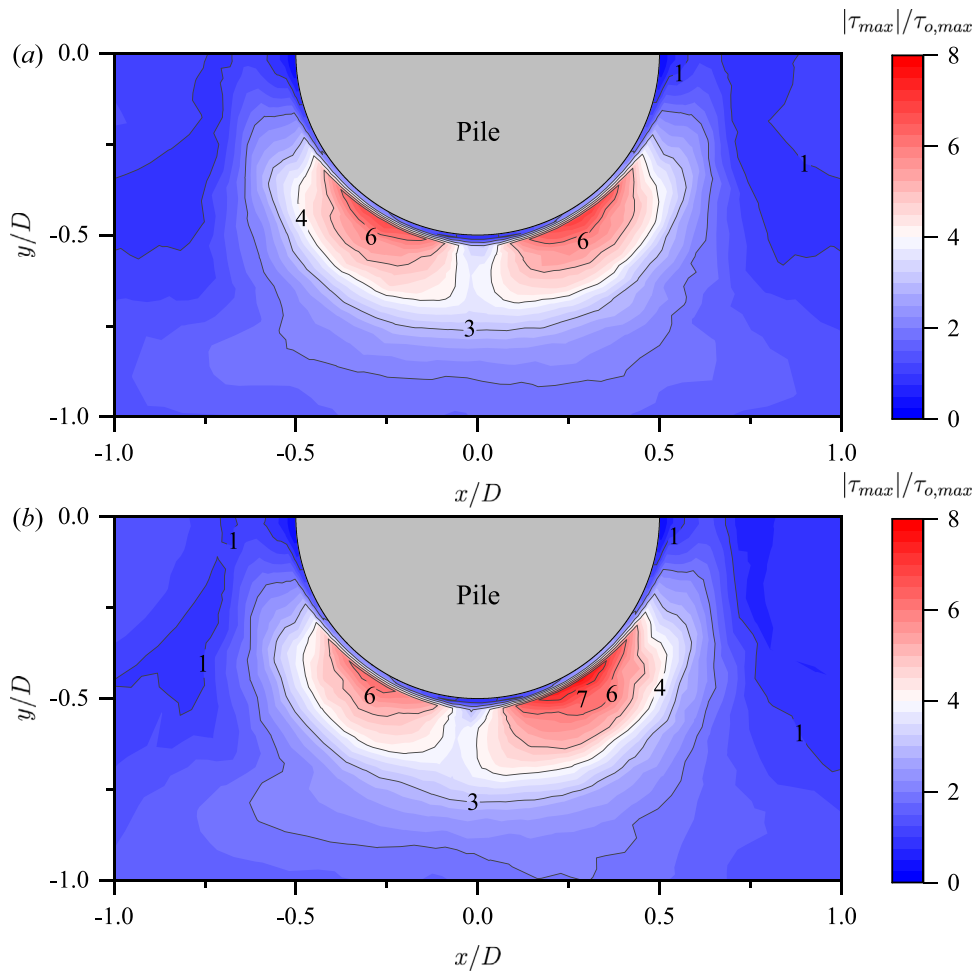


Fig. 13. Amplification of bed shear stress around the circular pile (a) without and (b) with considering the seepage.

flow velocity is decreasing. This is because of the enhanced suspended load transport, which will be discussed in Section 5.2. The rapid scour at the back of the pile during the end of tsunami draw-down was also reported in a large-scale experimental study on tsunami scour around a cylinder (Tonkin et al., 2003). Consequently, the temporary equilibrium scour depth with the seepage response increases by 16%, compared to the impermeable seabed.

Overall, the computed development of scour depth at the front, side, and back of the circular pile with seepage effects is very similar to the trends of experimental observations in Tonkin et al. (2003), which indicates the capability of the present CFD model in predicting the tsunami scour. Since the present numerical model does not take into account the variations of wave free surface, e.g., wave shoaling and breaking phenomena involved in their tests, a direct comparison with their experimental results is not feasible.

Fig. 15 presents the scour profiles along the center line of the circular pile with and without considering seepage effects. At $t/T = 0.25$ (see Fig. 15a), the scour hole in front of the pile ($x/D < 0$) has a slope angle $\beta = 31.4^\circ$ close to the angle of repose $\beta_r = 32^\circ$ of the sediment grains. The scour profiles almost overlap into a single line, owing to the indistinguishable horseshoe vortex with and without seepage, as discussed in Section 4.1. In contrast, the scour hole at the back of the pile ($x/D > 0$) is shallower in the presence of seabed suction, which is due to the decreased bed shear stress amplification underneath the lee-wake vortices as shown in Fig. 10(c), and the increased critical Shields parameter as shown in Fig. 7(b). At $t/T = 0.75$ (see Fig. 15b), the scour hole within the horseshoe vortex at the back of the pile ($x/D > 0$) marginally increases when considering the seepage. A sandbar forms

in front ($x/D < 0$) of the pile, and its formation and migration are due to the large-scale counter-rotating streamwise vortices in the lee wake (Baykal et al., 2015). When considering the seepage effect, the sandbar is more pronounced because of the enhanced deposition shown in Fig. 14.

Fig. 16 depicts the seabed topography around the circular pile with (lower panels) and without (upper panels) the seepage effects. At $t/T = 0.25$, a semi-circular scour hole with a steep slope forms around the upstream side of the circular pile, see Fig. 16(a,b). The sediment is deposited behind both sides of the pile, creating two sandbars with steeper slopes. A strip-like scour hole is visible between these two sandbars due to vortex shedding, trailing downstream (right-hand boundary side) of the pile. These scouring features are marginally less pronounced in the presence of seabed suction. At $t/T = 0.75$, the scour hole around the side and back of the pile deepens further following the flow reversal. As a result, the scour hole around the pile resembles an inverted frustum shape. Additionally, the sandbars behind the pile are eroded as they are more exposed to the approach flow, migrating upstream. The sediment is deposited into two sandbars alongside the pile. Moreover, the front scour hole is gradually backfilled. The backfilling and sandbars are more noticeable for the “seepage-on” scenario due to the increased scour at the pile back caused by the seabed injection. The erosion caused by the lee-wake vortices becomes visible in front of the pile.

The seepage response to the tsunami loading can affect the scour processes. The sediment redistribution caused by the seepage response can impact the main focus of scour protection in coastal and offshore areas, e.g., the rapid scour near the back of the monopile during the depression tsunami wave potentially leads to a foundation failure or bridge collapse.

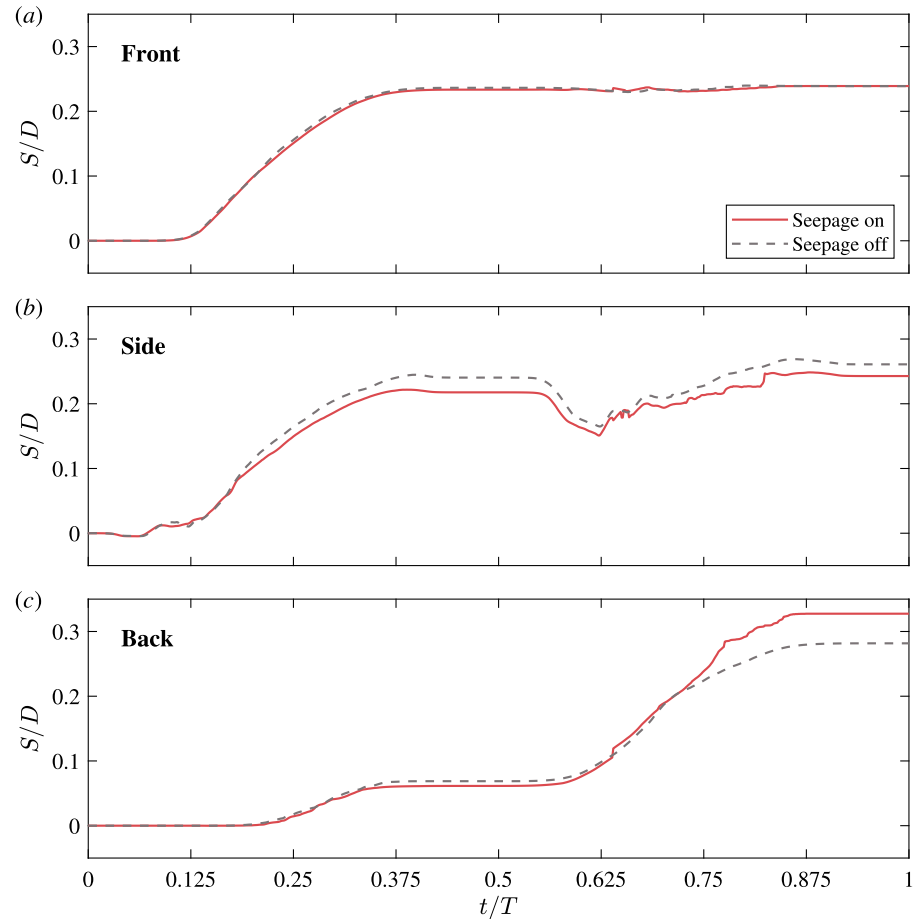


Fig. 14. Scour depth at the (a) front ($\phi = 0^\circ$), (b) side ($\phi = 90^\circ$), and (c) back ($\phi = 180^\circ$) of the circular pile without and with considering the seepage.

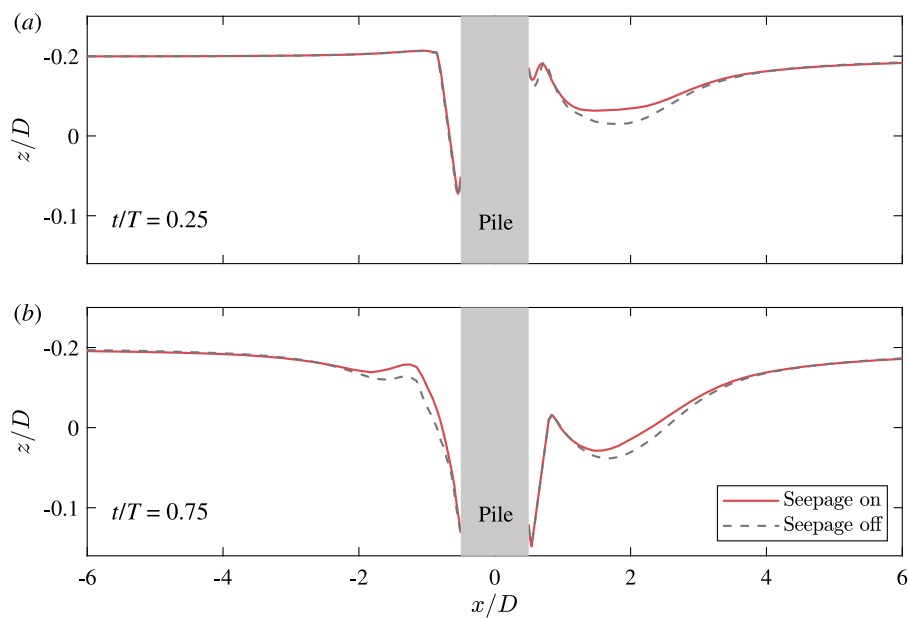


Fig. 15. Scour profiles along the center line of the circular pile at (a) $t/T = 0.25$ and (b) $t/T = 0.75$ without and with considering seepage effects.

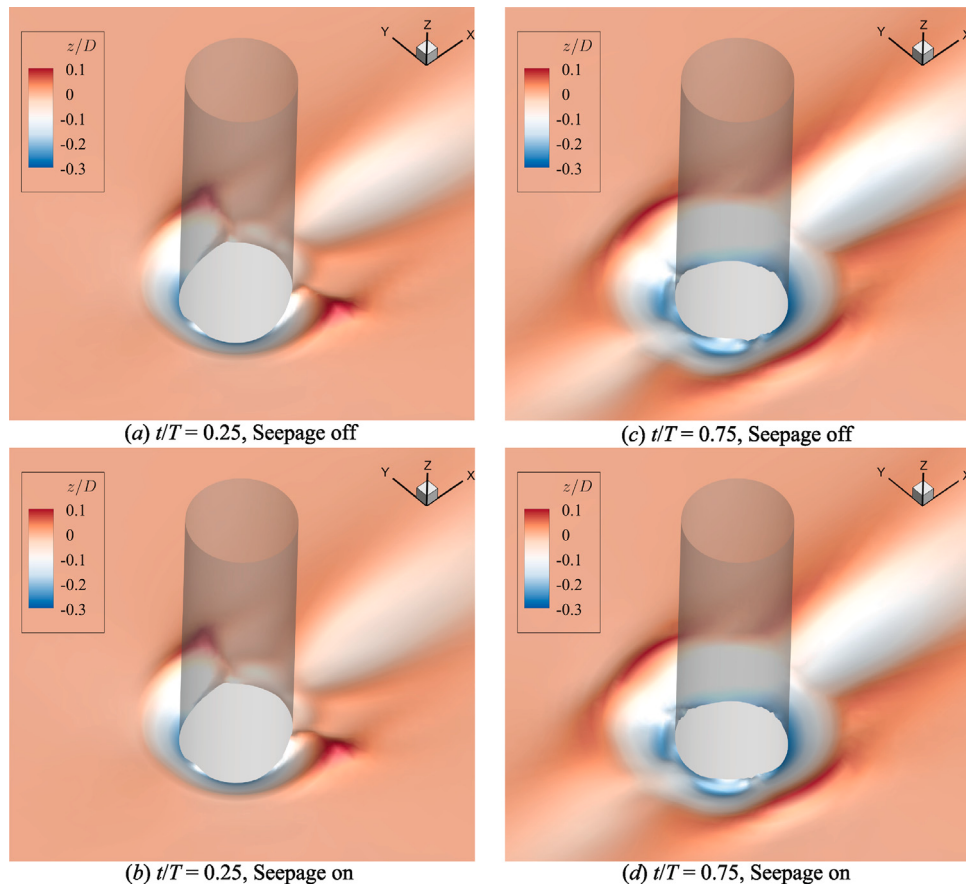


Fig. 16. Bed topography around the circular pile at $t/T = 0.25$ and $t/T = 0.75$ (a,c) without and (b,d) with considering seepage effects.

5.2. Tsunami-induced sediment transport rate

In the present simulations of the seabed morphological evolution, the hydrodynamic flow conditions and onset threshold of sediment transport evolve simultaneously and continuously because of the disturbance of the structure and variations of bed slopes. To further elucidate the seepage effects on the tsunami scour, we investigate the tsunami-induced sediment transport rate during the scour development with and without considering the seepage. Fig. 17 shows the temporal variation of bed, suspended, and total load transport rates q_b , q_s , and q_t at the front ($t/T < 0.5$) and back ($t/T > 0.5$) of the pile. During the elevation wave, the bed load transport rate at the front side of the pile is generally lower in the presence of seabed suction, as seen in Fig. 17(a). This is mainly due to the competing effects of seabed suction on the bed mobility discussed in Section 3, combined with the marginally weakened horseshoe vortex shown in Section 4.1. The suspended load transport rate is also generally decreased compared to the impermeable seabed, as illustrated in Fig. 17(b). Note that the suspended load transport dominates sediment transport during the full-scale tsunami propagation. Consequently, the total load transport rate is lower when considering the seepage response, as shown in Fig. 17(c). During the depression wave, the seabed injection intensifies the sediment transport at the back side of the pile, especially for the suspended load, as shown in Fig. 17(a,b). As a result, the total sediment transport increases when considering the seepage response in Fig. 17(c), which confirms the observation of Tonkin et al. (2003) and expectation of Yeh and Mason (2014).

Fig. 18 illustrates the overall picture of the instantaneous suspended load transport rate around the pile. At $t/T = 0.25$, the high suspended load transport rate is mainly concentrated on the front side of the pile as seen in Fig. 18(a,b) due to the combination of the horseshoe vortex

and the streamline contraction. It spreads out downstream, which is less noticeable in the presence of seabed suction for the simulated tsunami wave signal. At $t/T = 0.75$, the seabed injection increases the suspended load transport rate around the circular pile. However, the momentary liquefaction does not occur under the present tsunami and sediment conditions ($i/i_c < 1$, see Fig. 7a).

6. Conclusions

In the present study, we have examined the role of seepage response in full-scale tsunami-induced main flow features and scour around a circular pile. The onset threshold of sediment transport and the bed load transportation considering both bed-slope modifications and three-dimensional seepage forces are analyzed and implemented in the coupled hydrodynamic, morphological, and soil models. The main conclusions are drawn as follows:

In the rigid-bed simulations, we found that the seepage response can affect the main tsunami flow features in the presence of a circular pile, which determines the scour processes. The tsunami-induced vortical structures and bed shear stress amplification around the pile resemble the intermediate between wind-generated waves and a steady current. Seabed suction during the elevation wave can reduce the amplification of bed shear stress beneath the contracted streamlines alongside the pile and lee-wake vortices. In contrast, seabed injection during the depression wave increases the shear stress amplification. It advances the boundary layer separation point along the pile height, further altering the lee-wake vortices. The size of the horseshoe vortex and the upward-directed pressure gradient within it are minimally impacted by the seepage flows.

In the morphological simulations, our results suggest that the suspended sediment transport dominates the scour under full-scale tsunami

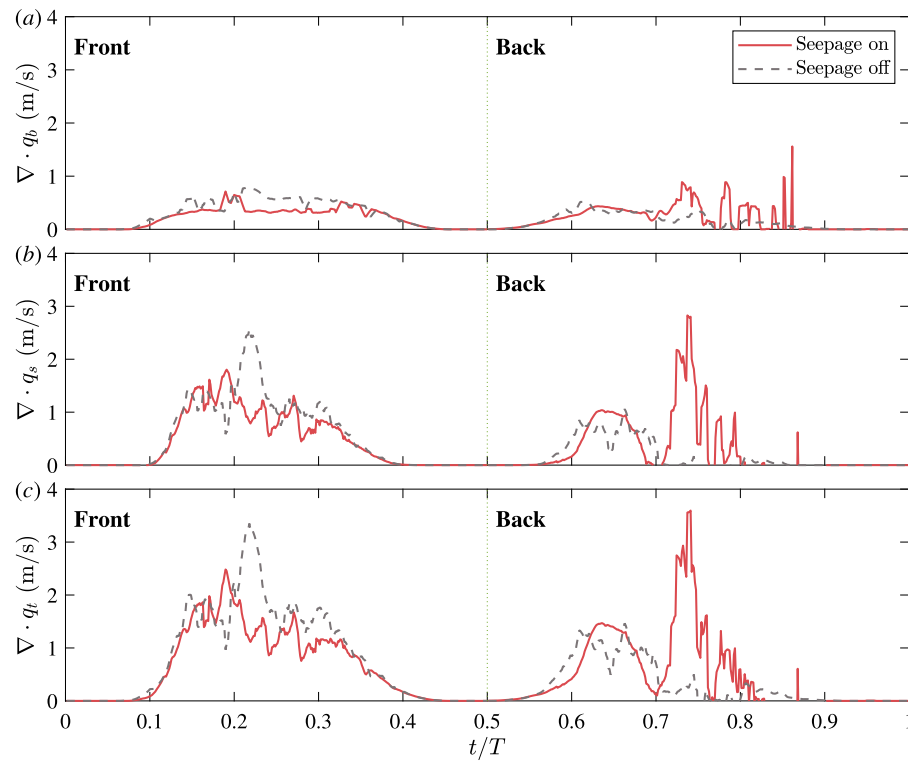


Fig. 17. Divergence of the (a) bed load transport rate q_b , (b) suspended load transport rate q_s , and (c) total load transport rate q_t at the front ($t/T < 0.5$) and back ($t/T > 0.5$) of the pile.

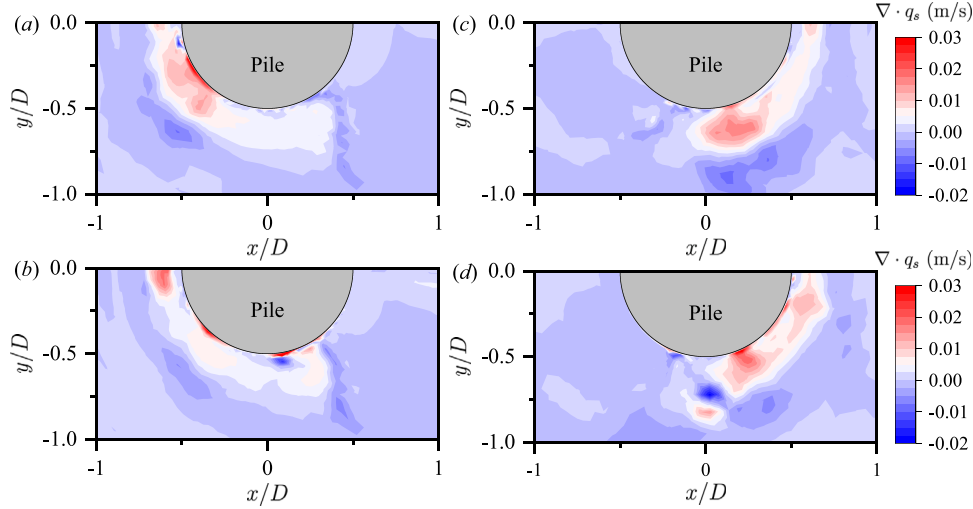


Fig. 18. Divergence of the suspended load transport rate around the circular pile (a,c) without and (b,d) with considering the seepage. The left panels are at $t/T = 0.25$, and the right panels are at $t/T = 0.75$.

waves. Seabed suction during the elevation wave can slightly reduce the sediment transport rate, decreasing the scour depth, especially at the pile side. Seabed injection during the depression wave does cause a more rapid and severe scour at the back of the pile, which is mainly due to the intensified suspended load transport. If only the bed load transport is considered, the effect of seepage on scour depth may not be obvious.

Our findings suggest that the seepage response should be considered when assessing full-scale tsunami-induced scour around a circular pile. The present model has several limitations. First, it does not account for the variability of the wave surface, which may not capture the full complexity of fluid dynamics affected by nearby structures

during tsunami events. Additionally, the model assumes that soil properties remain constant throughout the scour simulations, overlooking potential changes due to dynamic loading. Future studies will incorporate the effects of momentary liquefaction to better understand severe tsunami-induced scour processes.

CRediT authorship contribution statement

Zhengyu Hu: Writing – original draft, Visualization, Validation, Methodology, Investigation, Formal analysis, Data curation, Conceptualization. **Yuzhu Pearl Li:** Writing – review & editing, Supervision, Software, Resources, Project administration, Methodology, Investigation, Funding acquisition, Conceptualization.

Declaration of competing interest

The authors declare that they have no known competing financial interests or personal relationships that could have appeared to influence the work reported in this paper.

Acknowledgments

This project is funded by the Research, Innovation and Enterprise 2025 Coastal Protection and Flood Management Research Programme. The authors are grateful to the National Research Foundation of Singapore, PUB (Singapore's National Water Agency) for supporting this work done in the Coastal Protection and Flood Resilience Institute (CFI) Singapore under the project grant H1-P3. This study is partly supported by computational resources provided by the National Supercomputing Centre, Singapore (<https://www.nscc.sg>), under Project ID: 11002459.

Data availability

Data will be made available on request.

References

- Apotsos, A., Gelfenbaum, G., Jaffe, B., 2011. Process-based modeling of tsunami inundation and sediment transport. *J. Geophys. Res.: Earth Surf.* 116 (F1), <http://dx.doi.org/10.1029/2010JF001797>.
- Baker, C.J., 1979. The laminar horseshoe vortex. *J. Fluid Mech.* 95 (2), 347–367. <http://dx.doi.org/10.1017/S0022112079001506>.
- Baykal, C., Sumer, B.M., Fuhrman, D.R., Jacobsen, N.G., Fredsøe, J., 2015. Numerical investigation of flow and scour around a vertical circular cylinder. *Phil. Trans. R. Soc. A* 373 (2033), 20140104. <http://dx.doi.org/10.1098/rsta.2014.0104>.
- Baykal, C., Sumer, B.M., Fuhrman, D.R., Jacobsen, N.G., Fredsøe, J., 2017. Numerical simulation of scour and backfilling processes around a circular pile in waves. *Coast. Eng.* 122, 87–107. <http://dx.doi.org/10.1016/j.coastaleng.2017.01.004>.
- Biot, M.A., 1941. General theory of three-dimensional consolidation. *J. Appl. Phys.* 12 (2), 155–164. <http://dx.doi.org/10.1063/1.1712886>.
- Borrero, J.C., Cronin, S.J., Latu'ila, F.H., Tukuaftu, P., Heni, N., Tupou, A.M., Kula, T., Fa'anunu, O., Bosscherelle, C., Lane, E., Lynett, P., Kong, L., 2023. Tsunami runup and inundation in Tonga from the January 2022 eruption of Hunga volcano. *Pure Appl. Geophys.* 180 (1), 1–22. <http://dx.doi.org/10.1007/s00024-022-03215-5>.
- Bricker, J.D., Francis, M., Nakayama, A., 2012. Scour depths near coastal structures due to the 2011 Tohoku Tsunami. *J. Hydraul. Res.* 50 (6), 637–641. <http://dx.doi.org/10.1080/00221686.2012.721015>.
- Carrier, G.F., Wu, T.T., Yeh, H., 2003. Tsunami run-up and draw-down on a plane beach. *J. Fluid Mech.* 475, 79–99. <http://dx.doi.org/10.1017/S0022112002002653>.
- Cebeci, T., Chang, K.C., 1978. Calculation of incompressible rough-wall boundary-layer flows. *AIAA J.* 16 (7), 730–735. <http://dx.doi.org/10.2514/3.7571>.
- Chan, I.-C., Liu, P.L.F., 2012. On the runup of long waves on a plane beach. *J. Geophys. Res. Oceans* 117 (C8), <http://dx.doi.org/10.1029/2012JC007994>.
- Chen, X., Chiew, Y.-M., 2004. Velocity distribution of turbulent open-channel flow with bed suction. *J. Hydraul. Eng.* 130 (2), 140–148. [http://dx.doi.org/10.1061/\(ASCE\)0733-9429\(2004\)130:2\(140\)](http://dx.doi.org/10.1061/(ASCE)0733-9429(2004)130:2(140)).
- Chen, S.-g., Gong, E.-y., Zhao, X., Arikawa, T., Chen, X., 2022. Large-scale experimental study on scour around offshore wind monopiles under irregular waves. *Water Sci. Eng.* 15 (1), 40–46. <http://dx.doi.org/10.1016/j.wse.2021.12.003>.
- Chen, J., Huang, Z., Jiang, C., Deng, B., Long, Y., 2013. Tsunami-induced scour at coastal roadways: a laboratory study. *Nat. Hazards* 69 (1), 655–674. <http://dx.doi.org/10.1007/s11069-013-0727-6>.
- Chen, B., Li, S., 2018. Experimental study of local scour around a vertical cylinder under wave-only and combined wave-current conditions in a large-scale flume. *J. Hydraul. Eng.* 144 (9), 04018058. [http://dx.doi.org/10.1061/\(ASCE\)HY.1943-7900.0001502](http://dx.doi.org/10.1061/(ASCE)HY.1943-7900.0001502).
- Cheng, N.-S., Chiew, Y.-M., 1998. Modified logarithmic law for velocity distribution subjected to upward seepage. *J. Hydraul. Eng.* 124 (12), 1235–1241. [http://dx.doi.org/10.1061/\(ASCE\)0733-9429\(1998\)124:12\(1235\)](http://dx.doi.org/10.1061/(ASCE)0733-9429(1998)124:12(1235)).
- Cheng, N.-S., Chiew, Y.-M., 1999. Incipient sediment motion with upward seepage. *J. Hydraul. Res.* 37 (5), 665–681. <http://dx.doi.org/10.1080/00221689090498522>.
- Dawson, A.G., Shi, S., 2000. Tsunami deposits. *Pure Appl. Geophys.* 157 (6), 875–897. <http://dx.doi.org/10.1007/s000240050101>.
- Dey, S., Nath, T.K., 2010. Turbulence characteristics in flows subjected to boundary injection and suction. *J. Eng. Mech.* 136 (7), 877–888. [http://dx.doi.org/10.1061/\(ASCE\)EM.1943-7889.0000124](http://dx.doi.org/10.1061/(ASCE)EM.1943-7889.0000124).
- Engelund, F., Fredsøe, J., 1976. A sediment transport model for straight alluvial channels. *Hydrol. Res.* 7 (5), 293–306. <http://dx.doi.org/10.2166/nh.1976.0019>.
- Fernandez Luque, R., Van Beek, R., 1976. Erosion and transport of bed-load sediment. *J. Hydraul. Res.* 14 (2), 127–144. <http://dx.doi.org/10.1080/00221687609499677>.
- Fredsøe, J., Deigaard, R., 1992. *Mechanics of Coastal Sediment Transport*. World Scientific, Singapore.
- Fritz, H.M., Kongko, W., Moore, A., McAdoo, B., Goff, J., Harbitz, C., Uslu, B., Kalligeris, N., Suteja, D., Kalsum, K., Titov, V., Gusman, A., Latiif, H., Santoso, E., Sujoko, S., Djulkarnaen, D., Sunendar, H., Synolakis, C., 2007. Extreme runup from the 17 July 2006 Java tsunami. *Geophys. Res. Lett.* 34 (12), <http://dx.doi.org/10.1029/2007GL029404>.
- Fuhrman, D.R., Baykal, C., Sumer, B.M., Jacobsen, N.G., Fredsøe, J., 2014. Numerical simulation of wave-induced scour and backfilling processes beneath submarine pipelines. *Coast. Eng.* 94, 10–22. <http://dx.doi.org/10.1016/j.coastaleng.2014.08.009>.
- Guan, D.-w., Xie, Y.-x., Yao, Z.-s., Chiew, Y.-M., Zhang, J.-s., Zheng, J.-h., 2022. Local scour at offshore windfarm monopile foundations: A review. *Water Sci. Eng.* 15 (1), 29–39. <http://dx.doi.org/10.1016/j.wse.2021.12.006>.
- Guo, Z., Jeng, D.-S., Zhao, H., Guo, W., Wang, L., 2019. Effect of seepage flow on sediment incipient motion around a free spanning pipeline. *Coast. Eng.* 143, 50–62. <http://dx.doi.org/10.1016/j.coastaleng.2018.10.012>.
- Gupta, B.K., Basu, D., 2020. Offshore wind turbine monopile foundations: Design perspectives. *Ocean Eng.* 213, 107514. <http://dx.doi.org/10.1016/j.oceaneng.2020.107514>.
- Hjorth, P., 1975. *Studies on the Nature of Local Scour*. Lund Institute of Technology, University of Lund, Lund.
- Hu, Z., Huang, L., Li, Y., 2023. Fully-coupled hydroelastic modeling of a deformable wall in waves. *Coast. Eng.* 179, 104245. <http://dx.doi.org/10.1016/j.coastaleng.2022.104245>.
- Hu, Z., Li, Y., 2023. Two-dimensional simulations of large-scale violent breaking wave impacts on a flexible wall. *Coast. Eng.* 185, 104370. <http://dx.doi.org/10.1016/j.coastaleng.2023.104370>.
- Hu, Z., Qi, W.-G., Li, Y., 2024. The role of dynamic seepage response in sediment transport and tsunami-induced scour. *J. Geophys. Res. Oceans* (revised and resubmitted for publication).
- Hunt, J.C., Wray, A.A., Moin, P., 1988. Eddies, streams, and convergence zones in turbulent flows. In: *Proceedings of the Summer Program 1988*. Cent. Turbul. Res, Stanford, CA, pp. 193–208.
- Issa, R.I., 1986. Solution of the implicitly discretised fluid flow equations by operator-splitting. *J. Comput. Phys.* 62 (1), 40–65. [http://dx.doi.org/10.1016/0021-9991\(86\)90099-9](http://dx.doi.org/10.1016/0021-9991(86)90099-9).
- Jacobsen, N.G., 2011. *A Full Hydro- and Morphodynamic Description of Breaker Bar Development* (Ph.D. thesis). Technical University of Denmark.
- Jacobsen, N.G., Fredsøe, J., Jensen, J.H., 2014. Formation and development of a breaker bar under regular waves. Part 1: Model description and hydrodynamics. *Coast. Eng.* 88, 182–193. <http://dx.doi.org/10.1016/j.coastaleng.2013.12.008>.
- Jayaratne, M.P.R., Premaratne, B., Adewale, A., Mikami, T., Matsuba, S., Shibayama, T., Esteban, M., Nistor, I., 2016. Failure mechanisms and local scour at coastal structures induced by tsunami. *Coast. Eng. J.* 58 (04), 1640017. <http://dx.doi.org/10.1016/10.1142/s0578563416400179>.
- Keulegan, G.H., Carpenter, L.H., 1958. Forces on cylinders and plates in an oscillating fluid. *J. Res. Natl. Bur. Stand.* 60 (5), 423–440.
- Lacy, J.R., Rubin, D.M., Buscombe, D., 2012. Currents, drag, and sediment transport induced by a tsunami. *J. Geophys. Res. Oceans* 117 (C9), <http://dx.doi.org/10.1029/2012JC007954>.
- Larsen, B.E., Arbøll, L.K., Kristoffersen, S.F., Carstensen, S., Fuhrman, D.R., 2018. Experimental study of tsunami-induced scour around a monopile foundation. *Coast. Eng.* 138, 9–21. <http://dx.doi.org/10.1016/j.coastaleng.2018.04.007>.
- Larsen, B.E., Fuhrman, D.R., 2019a. Full-scale CFD simulation of tsunamis. Part 1: Model validation and run-up. *Coast. Eng.* 151, 22–41. <http://dx.doi.org/10.1016/j.coastaleng.2019.04.012>.
- Larsen, B.E., Fuhrman, D.R., 2019b. Full-scale CFD simulation of tsunamis. Part 2: Boundary layers and bed shear stresses. *Coast. Eng.* 151, 42–57. <http://dx.doi.org/10.1016/j.coastaleng.2019.04.011>.
- Larsen, B.E., Fuhrman, D.R., 2023. Re-parameterization of equilibrium scour depths and time scales for monopiles. *Coast. Eng.* 185, 104356. <http://dx.doi.org/10.1016/j.coastaleng.2023.104356>.
- Larsen, B.E., Fuhrman, D.R., Baykal, C., Sumer, B.M., 2017. Tsunami-induced scour around monopile foundations. *Coast. Eng.* 129, 36–49. <http://dx.doi.org/10.1016/j.coastaleng.2017.08.002>.
- Li, Y., Ong, M.C., Fuhrman, D.R., 2020a. CFD investigations of scour beneath a submarine pipeline with the effect of upward seepage. *Coast. Eng.* 156, 103624. <http://dx.doi.org/10.1016/j.coastaleng.2019.103624>.
- Li, Y., Ong, M.C., Fuhrman, D.R., Larsen, B.E., 2020b. Numerical investigation of wave-plus-current induced scour beneath two submarine pipelines in tandem. *Coast. Eng.* 156, 103619. <http://dx.doi.org/10.1016/j.coastaleng.2019.103619>.
- Li, Y., Ong, M.C., Tang, T., 2018. Numerical analysis of wave-induced poro-elastic seabed response around a hexagonal gravity-based offshore foundation. *Coast. Eng.* 136, 81–95. <http://dx.doi.org/10.1016/j.coastaleng.2018.02.005>.
- Li, Y., Ong, M.C., Tang, T., 2020c. A numerical toolbox for wave-induced seabed response analysis around marine structures in the OpenFOAM® framework. *Ocean Eng.* 195, 106678. <http://dx.doi.org/10.1016/j.oceaneng.2019.106678>.

- Liu, P.L.F., Higuera, P., 2022. Water waves generated by moving atmospheric pressure: theoretical analyses with applications to the 2022 Tonga event. *J. Fluid Mech.* 951, A34. <http://dx.doi.org/10.1016/10.1017/jfm.2022.840>.
- Li, P.L.F., Park, Y.S., Lara, J.L., 2007. Long-wave-induced flows in an unsaturated permeable seabed. *J. Fluid Mech.* 586, 323–345. <http://dx.doi.org/10.1017/S0022112007007057>.
- Lynett, P., McCann, M., Zhou, Z., Renteria, W., Borrero, J., Greer, D., Fa'anunu, O., Bosserelle, C., Jaffe, B., La Selle, S., Ritchie, A., Snyder, A., Nasr, B., Bott, J., Graehl, N., Synolakis, C., Ebrahimi, B., Cinar, G.E., 2022. Diverse tsunamigenesis triggered by the Hunga Tonga-Hunga Ha'apai eruption. *Nature* 609 (7928), 728–733. <http://dx.doi.org/10.1038/s41586-022-05170-6>.
- Madsen, P.A., Fuhrman, D.R., Schäffer, H.A., 2008. On the solitary wave paradigm for tsunamis. *J. Geophys. Res. Oceans* 113 (C12), <http://dx.doi.org/10.1029/2008JC004932>.
- McGovern, D.J., Todd, D., Rossetto, T., Whitehouse, R.J.S., Monaghan, J., Gomes, E., 2019. Experimental observations of tsunami induced scour at onshore structures. *Coast. Eng.* 152, 103505. <http://dx.doi.org/10.1016/j.coastaleng.2019.103505>.
- Mori, N., Takahashi, T., Yasuda, T., Yanagisawa, H., 2011. Survey of 2011 Tohoku earthquake tsunami inundation and run-up. *Geophys. Res. Lett.* 38 (7), <http://dx.doi.org/10.1029/2011GL049210>.
- Nakamura, T., Kuramitsu, Y., Mizutani, N., 2008. Tsunami scour around a square structure. *Coast. Eng. J.* 50 (2), 209–246. <http://dx.doi.org/10.1142/S057856340800179X>.
- Omira, R., Ramalho, R.S., Kim, J., González, P.J., Kadri, U., Miranda, J.M., Carrilho, F., Baptista, M.A., 2022. Global Tonga tsunami explained by a fast-moving atmospheric source. *Nature* 609 (7928), 734–740. <http://dx.doi.org/10.1038/s41586-022-04926-4>.
- Patankar, S.V., Spalding, D.B., 1972. A calculation procedure for heat, mass and momentum transfer in three-dimensional parabolic flows. *Int. J. Heat Mass Transfer* 15 (10), 1787–1806. [http://dx.doi.org/10.1016/0017-9310\(72\)90054-3](http://dx.doi.org/10.1016/0017-9310(72)90054-3).
- Qi, W.-G., Gao, F.-P., 2014. Physical modeling of local scour development around a large-diameter monopile in combined waves and current. *Coast. Eng.* 83, 72–81. <http://dx.doi.org/10.1016/j.coastaleng.2013.10.007>.
- Qi, W.-G., Gao, F.-P., 2018. Wave induced instantaneously-liquefied soil depth in a non-cohesive seabed. *Ocean Eng.* 153, 412–423. <http://dx.doi.org/10.1016/j.oceaneng.2018.01.107>.
- Ren, Z., Higuera, P., Liu, P.L.F., 2023. On tsunami waves induced by atmospheric pressure shock waves after the 2022 Hunga Tonga-Hunga Ha'apai volcano eruption. *J. Geophys. Res. Oceans* 128 (4), e2022JC019166, <https://doi.org/10.1029/2022JC019166>.
- Robbe-Saule, M., Morize, C., Henaff, R., Bertho, Y., Sauret, A., Gondret, P., 2021. Experimental investigation of tsunami waves generated by granular collapse into water. *J. Fluid Mech.* 907, A11. <http://dx.doi.org/10.1016/10.1017/jfm.2020.807>.
- Roulund, A., Sumer, B.M., Fredsøe, J., Michelsen, J., 2005. Numerical and experimental investigation of flow and scour around a circular pile. *J. Fluid Mech.* 534, 351–401. <http://dx.doi.org/10.1017/S0022112005004507>.
- Sarlin, W., Morize, C., Sauret, A., Gondret, P., 2021. Nonlinear regimes of tsunami waves generated by a granular collapse. *J. Fluid Mech.* 919, R6. <http://dx.doi.org/10.1016/10.1017/jfm.2021.400>.
- Satake, K., Bourgeois, J., Abe, K., Abe, K., Tsuji, Y., Imamura, F., Lio, Y., Katao, H., Noguera, E., Estrada, F., 1993. Tsunami field survey of the 1992 Nicaragua earthquake. *EOS Trans. Am. Geophys. Union* 74 (13), 145–157. <http://dx.doi.org/10.1029/93EO00271>.
- Sharma, A., Kumar, B., 2017. Structure of turbulence over non uniform sand bed channel with downward seepage. *Eur. J. Mech. B* 65, 530–551. <http://dx.doi.org/10.1016/j.euromechflu.2017.05.006>.
- Sugawara, D., Goto, K., Jaffe, B.E., 2014. Numerical models of tsunami sediment transport — Current understanding and future directions. *Mar. Geol.* 352, 295–320. <http://dx.doi.org/10.1016/j.margeo.2014.02.007>.
- Sui, T., Liu, C., Zhang, J., Zhang, C., Zheng, J., 2024. 3D numerical modeling of wave-monopile-seabed interaction in the presence of a scour hole. *Ocean Eng.* 298, 117254. <http://dx.doi.org/10.1016/j.oceaneng.2024.117254>.
- Sui, T., Staunstrup, L.H., Carstensen, S., Fuhrman, D.R., 2021. Span shoulder migration in three-dimensional current-induced scour beneath submerged pipelines. *Coast. Eng.* 164, 103776. <http://dx.doi.org/10.1016/j.coastaleng.2020.103776>.
- Sumer, B.M., 2006. *Hydrodynamics around Cylindrical Structures*. World Scientific.
- Sumer, B.M., 2014. Liquefaction Around Marine Structures. World Scientific, <http://dx.doi.org/10.1142/7986>.
- Sumer, B.M., Christiansen, N., Fredsøe, J., 1997. The horseshoe vortex and vortex shedding around a vertical wall-mounted cylinder exposed to waves. *J. Fluid Mech.* 332, 41–70. <http://dx.doi.org/10.1017/S0022112096003898>.
- Sumer, B.M., Fredsøe, J., 2001. Scour around pile in combined waves and current. *J. Hydraul. Eng.* 127 (5), 403–411. [http://dx.doi.org/10.1061/\(ASCE\)0733-9429\(2001\)127:5\(403\)](http://dx.doi.org/10.1061/(ASCE)0733-9429(2001)127:5(403).
- Sumer, B.M., Fredsøe, J., 2002. *The Mechanics of Scour in the Marine Environment*. World Scientific.
- Sumer, B.M., Fredsøe, J., Christiansen, N., 1992. Scour around vertical pile in waves. *J. Waterw. Port, Coast. Ocean Eng.* 118 (1), 15–31. [http://dx.doi.org/10.1061/\(ASCE\)0733-950X\(1992\)118:1\(15\)](http://dx.doi.org/10.1061/(ASCE)0733-950X(1992)118:1(15).
- Sumer, B.M., Petersen, T.U., Locatelli, L., Fredsøe, J., Musumeci, R.E., Foti, E., 2013. Backfilling of a scour hole around a pile in waves and current. *J. Waterw. Port, Coast. Ocean Eng.* 139 (1), 9–23. [http://dx.doi.org/10.1061/\(ASCE\)WW.1943-5460.0000161](http://dx.doi.org/10.1061/(ASCE)WW.1943-5460.0000161).
- Taye, J., Sharma, A., Kumar, B., 2023. Effect of downward seepage on turbulence and morphology in mobile boundary sinuous channel. *Phys. Fluids* 35 (1), <http://dx.doi.org/10.1063/5.0133201>.
- Tong, L., Liu, P.L.F., 2022. Transient wave-induced pore-water-pressure and soil responses in a shallow unsaturated poroelastic seabed. *J. Fluid Mech.* 938, A36. <http://dx.doi.org/10.1017/jfm.2022.184>.
- Tonkin, S., Yeh, H., Kato, F., Sato, S., 2003. Tsunami scour around a cylinder. *J. Fluid Mech.* 496, 165–192. <http://dx.doi.org/10.1017/S0022112003006402>.
- Van Driest, E.R., 1956. On turbulent flow near a wall. *J. Aeronaut. Sci.* 23 (11), 1007–1011. <http://dx.doi.org/10.2514/8.3713>.
- Wang, Z., Pan, J., Xie, D., Zhang, C., Sui, T., 2024. Influence of cnoidal wave-induced seepage force on shields number in shallow water. *Ocean Eng.* 310, 118690. <http://dx.doi.org/10.1016/j.oceaneng.2024.118690>.
- Whitehouse, R.J.S., Stroescu, E.I., 2023. Scour depth development at piles of different height under the action of cyclic (tidal) flow. *Coast. Eng.* 179, 104225. <http://dx.doi.org/10.1016/j.coastaleng.2022.104225>.
- Wilcox, D.C., 2006. *Turbulence Modeling for CFD*, third ed. DCW Industries.
- Wilcox, D.C., 2008. Formulation of the $k-\omega$ turbulence model revisited. *AIAA J.* 46 (11), 2823–2838. <http://dx.doi.org/10.2514/1.36541>.
- Williams, I.A., Fuhrman, D.R., 2016. Numerical simulation of tsunami-scale wave boundary layers. *Coast. Eng.* 110, 17–31. <http://dx.doi.org/10.1016/j.coastaleng.2015.12.002>.
- Wilson, R., Davenport, C., Jaffe, B., 2012. Sediment scour and deposition within harbors in California (USA), caused by the March 11, 2011 Tohoku-oki tsunami. *Sediment. Geol.* 282, 228–240. <http://dx.doi.org/10.1016/j.sedgeo.2012.06.001>.
- Ye, J., Zhou, H., He, K., 2024. A generalized framework of two-way coupled numerical model for fluid-structure-seabed interaction (FSSI): Explicit algorithm. *Eng. Geol.* 340, 107679. <http://dx.doi.org/10.1016/j.enggeo.2024.107679>.
- Yeh, H., Mason, H., 2014. Sediment response to tsunami loading: mechanisms and estimates. *Géotechnique* 64 (2), 131–143. <http://dx.doi.org/10.1680/geot.13.P.033>.
- Yeh, H., Sato, S., Tajima, Y., 2013. The 11 March 2011 east Japan earthquake and tsunami: Tsunami effects on coastal infrastructure and buildings. *Pure Appl. Geophys.* 170 (6), 1019–1031. <http://dx.doi.org/10.1007/s00024-012-0489-1>.
- Yoshii, T., Tanaka, S., Matsuyama, M., 2017. Tsunami deposits in a super-large wave flume. *Mar. Geol.* 391, 98–107. <http://dx.doi.org/10.1016/j.margeo.2017.07.020>.
- Yoshii, T., Tanaka, S., Matsuyama, M., 2018. Tsunami inundation, sediment transport, and deposition process of tsunami deposits on coastal lowland inferred from the Tsunami Sand Transport Laboratory Experiment (TSTLE). *Mar. Geol.* 400, 107–118. <http://dx.doi.org/10.1016/j.margeo.2018.03.007>.
- Zhai, H., Jeng, D.-S., 2022. Two-way coupling model for wave-induced oscillatory soil response around marine structures. *Ocean Eng.* 249, 110791. <http://dx.doi.org/10.1016/j.oceaneng.2022.110791>.
- Zhai, H., Jeng, D.-S., 2024. Impacts of wave-induced seabed response on local scour around a pipeline: PORO-FSSI-SCOUR-FOAM. *Coast. Eng.* 187, 104424. <http://dx.doi.org/10.1016/j.coastaleng.2023.104424>.
- Zhai, H., Jeng, D.-S., Guo, Z., Liang, Z., 2021a. Impact of two-dimensional seepage flow on sediment incipient motion under waves. *Appl. Ocean Res.* 108, 102510. <http://dx.doi.org/10.1016/j.apor.2020.102510>.
- Zhai, H., Jeng, D.-S., Guo, Z., Sui, T., 2021b. Modified Shields number for sediment incipient motion around a pile with impact of three-dimensional seepage in a porous seabed. *Appl. Ocean Res.* 117, 102896. <http://dx.doi.org/10.1016/j.apor.2021.102896>.
- Zhang, S., Li, B., Ma, H., 2023. Numerical investigation of scour around the monopile using CFD-DEM coupling method. *Coast. Eng.* 183, 104334. <http://dx.doi.org/10.1016/j.coastaleng.2023.104334>.
- Zhao, M., Cheng, L., 2008. Numerical modeling of local scour below a piggyback pipeline in currents. *J. Hydraul. Eng.* 134 (10), 1452–1463. [http://dx.doi.org/10.1061/\(ASCE\)0733-9429\(2008\)134:10\(1452\)](http://dx.doi.org/10.1061/(ASCE)0733-9429(2008)134:10(1452).
- Zhao, M., Cheng, L., Zang, Z., 2010. Experimental and numerical investigation of local scour around a submerged vertical circular cylinder in steady currents. *Coast. Eng.* 57 (8), 709–721. <http://dx.doi.org/10.1016/j.coastaleng.2010.03.002>.
- Zou, X., Cao, X., Zhou, C., Zhou, M., Zhang, X., 2021. Experimental study on the bearing capacity of large-diameter monopile in sand under water flow condition. *Ocean Eng.* 224, 108708. <http://dx.doi.org/10.1016/j.oceaneng.2021.108708>.